

UNIVERSITY OF CALGARY

# IMAGING BELOW DIPPING ANISOTROPIC STRATA

by

Robert W. Vestrum

A THESIS

SUBMITTED TO THE FACULTY OF GRADUATE STUDIES

IN PARTIAL FULFILLMENT OF THE REQUIREMENTS

FOR THE DEGREE OF DOCTOR OF PHILOSOPHY

DEPARTMENT OF GEOLOGY AND GEOPHYSICS

CALGARY, ALBERTA

JULY 2003

© Robert W. Vestrum 2003



UNIVERSITY OF CALGARY  
FACULTY OF GRADUATE STUDIES

The undersigned certify that they have read, and recommend to the Faculty of Graduate Studies for acceptance, a thesis entitled “Imaging Below Dipping Anisotropic Strata” submitted by Robert W. Vestrum in partial fulfillment of the requirements for the degree of Doctor of Philosophy.

---

Supervisor, D.C. Lawton, Geology and Geophysics

---

L.R. Lines, Geology and Geophysics

---

R.J. Brown, Geology and Geophysics

---

B.J. Moorman, Geology and Geophysics

---

External Examiner, D.R. Schmitt, University of Alberta

---

Date



# Abstract

A historical account of research into seismic anisotropy and research into seismic migration illustrates the progression of geophysical study towards identifying and solving the problem of imaging geologic structures beneath dipping anisotropic strata. With this goal in mind, I developed an anisotropic depth migration algorithm and methodology, demonstrated its effectiveness at correcting for imaging and positioning problems on seismic data, and applied this technology in reducing oil-and-gas exploration risk.

Numerical modelling predicted that the lateral-position error on structures below dipping anisotropic strata would be a maximum when the overburden dip is near  $45^\circ$ . The magnitude of the lateral-position error is approximately equal to Thomsen's anisotropic parameter  $\epsilon$  multiplied by the thickness of the dipping anisotropic strata. The other anisotropic effect I modelled was the smear effect, where different source-receiver offsets image the same structure at different locations, thereby smearing the structural image. The smear is larger than Thomsen's  $\epsilon$  multiplied by the thickness of the anisotropic overburden for dips between  $15^\circ$  and  $30^\circ$ .

For algorithm development, I modified a Kirchhoff migration algorithm already in use for seismic imaging in the Canadian thrust belt to handle corrections for seismic velocity anisotropy. Further modification of the velocity-model-building tools allow the creation of anisotropic velocity models for depth migration. Anisotropic velocity model building involves definition of the geologic dip and Thomsen's anisotropic constants. Traditional migration-velocity diagnostics guide the interpretation of the anisotropic velocity model.

Three case histories that apply the methodologies developed for this thesis illustrate the improvements in position accuracy and imaging of subsurface structures when anisotropic effects are corrected in depth migration. The final case history addresses the ultimate purpose of this research: to reduce risk in hydrocarbon exploration. The location for a natural-gas development well was chosen from seismic sections processed using the assumption of isotropic velocities. Drilling in front of the leading edge of the exploration target revealed the incorrect position of the target structure on these processed seismic data. Anisotropic depth migration positioned the subsurface structure accurately. The structural position interpreted on the new seismic section led to additional drilling on the structure and a successful natural-gas well.



# Acknowledgments

First and foremost, I wish to thank my wife Tammy for her support of my studies over twelve of our fifteen years of marriage. A natural manager, she has directed my education and career, provided invaluable feedback for improving my lectures, and kept me focussed on our long-term goals. Next, I turn to our six stress-relieving distractions, RJ, Aaron, Alex, Zoë, Sarah, and Louellen, who bring balance to my life and help me stay enthused about science.



To Don Lawton I owe a debt of gratitude for his help in my escape from drowning in big-oil mediocrity to pursue PhD studies. Brian Link, of Kelman Technologies Inc, was also instrumental in instigating this project. All service-company managers that I talked to saw little potential in anisotropic depth migration with the exception of Brian Link.

Kelman Technologies also deserves recognition for financial support of this research and for allowing me to tinker with their processing system during my own software development. Veritas GeoServices also supported this work in its later stages and now gives me the opportunity to pursue anisotropic depth migration in 3D. Other financial support in the early stages came from the National Science and Engineering Research Council and throughout from the sponsors of the Fold/Fault Research Project at the University of Calgary.

Seismic data from thrust-belt exploration was an essential ingredient in the testing of algorithms and model-building strategies. Thanks go to Husky Energy and Talisman Energy for the Benjamin Creek benchmark dataset, to Amoco Canada, and to Suncor Energy for permission to publish the exploration case history.

Other individuals that played key roles in this research are Kai Muenzer from Shell Canada, Rick Steele and Ron Schmid from Kelman, Al Petrella from Veritas, and Clair Callahan from Suncor.

Finally, thanks to my examining committee for their constructive edits, to Doug Schmitt of the University of Alberta for sharing his passion for anisotropy research, and to Jim Brown of the University of Calgary for the theoretical foundation in anisotropy he gave me in my MSc studies.





# Table of Contents

Approval page .....	ii
Abstract .....	iii
Acknowledgments .....	iv
Table of Contents .....	v
List of Table .....	vi
List of Figures .....	vii
<b>Chapter 1: Introduction .....</b>	<b>1</b>
1.1 Seismic velocity anisotropy .....	1
1.2 Seismic migration .....	5
1.2.1 Time migration .....	5
1.2.2 Depth migration .....	5
1.2.3 Anisotropic depth migration .....	7
1.2.4 Migration velocity analysis .....	7
1.3 History of anisotropic migration research .....	9
1.3.1 Problem definition .....	10
1.3.2 Algorithm design .....	11
1.3.3 Practical applications .....	13
1.3.4 Conclusions from the historical account .....	16
1.4 Structure of thesis .....	17
<b>Chapter 2: Anisotropic depth migration .....</b>	<b>19</b>
2.1 Model definition .....	20
2.1.1 The sideslip effect .....	20
2.1.2 Offset-dependent sideslip .....	23
2.1.3 The anisotropic velocity model .....	26
2.2 Algorithm implementation .....	26
2.3 Algorithm testing .....	29
2.4 Summary .....	31
<b>Chapter 3: Velocity model building .....</b>	<b>33</b>
3.1 The velocity model .....	33
3.2 Image-gather analysis .....	35
3.3 Stack-image analysis .....	37
3.4 Directional image gathers .....	39
3.4.1 Physical-model data example .....	42
3.4.2 Field data example .....	43
3.5 Summary .....	44
<b>Chapter 4: Case Histories .....</b>	<b>47</b>
4.1 Benjamin Creek .....	47
4.2 The Triangle Zone .....	49
4.2.1 Velocity models .....	49
4.2.2 Migrated sections .....	51
4.3 The Nordegg sidetrack .....	53
4.3.1 Drilling well B .....	55
4.3.2 Discussion .....	56
4.4 Conclusions .....	59
<b>Chapter 5: Conclusions .....</b>	<b>61</b>
<b>References .....</b>	<b>63</b>



# List of Table

4.1	Preprocessing steps used in data preparation for prestack depth migration. ....	48
-----	---	----



# List of Figures

1.1	Transversely isotropic (TI) medium with a vertical axis of symmetry. The seismic velocity is equal in all directions parallel to bedding and lower perpendicular to bedding. ....	2
1.2	A TTI medium is a TI medium with a symmetry axis of arbitrary tilt. ....	3
1.3	Aplanatic surface for a time migration assuming homogeneous, isotropic media. ....	6
1.4	Aplanatic surface for a traditional depth migration that corrects for lateral velocity heterogeneity but assumes velocity isotropy. ....	6
1.5	Aplanatic surface for an anisotropic depth migration that corrects for velocity anisotropy. The skewed shape of the surface corrects for the sideslip effect. Dip is shown by $\phi$ . ....	7
1.6	Aplanatic surface for an anisotropic depth migration that corrects for both raybending caused by lateral velocity changes and sideslip caused by seismic anisotropy. ....	8
1.7	Prestack migrated image gathers after Zhu et al. (1998). (a) was migrated with too low an input velocity, (c) was migrated with too high an input velocity, and (b) was migrated with the correct input velocity. ....	8
1.8	Reflection back and forth oblique to the wave normal defined by perpendicular distance (after Musgrave, 1959). ....	10
1.9	Isotropic time migrations of numerical-model seismic data from Alkhalifah and Larner (1994). (a) has an isotropic model and (b) uses an anisotropic model with $\epsilon = 0.11$ , $\delta = -0.035$ , and a $30^\circ$ tilted symmetry axis. Note the lateral position change between (a) and (b) of the horizontal reflectors. (c) shows a graph of positioning error versus reflector dip with a tilt of the anisotropic symmetry axis, $\phi$ , of $30^\circ$ (after Alkhalifah and Larner, 1994). ....	12
1.10	Migrated image of ultrasonic-pulse transmission experiment (after Isaac and Lawton, 1999). Distance measurements are scaled 1:10000 from the laboratory setup. ....	14
1.11	(a) Anisotropic physical model and (b) corresponding time-migrated seismic section. Note the lateral position error on the seismic image of 290 m resulting from the sideslip effect (after Isaac and Lawton, 1999). ....	15



2.1	Waves propagating across dipping anisotropic strata separated by $\Delta t$ . The grey lines represent the $45^\circ$ dip orientation. The lateral distance between the source and the reflection point is the sideslip distance $S$ for a zero-offset reflection. ....	20
2.2	Normalized sideslip distance, $S/Z$ , for a zero-offset trace as a function of dip of the anisotropic overburden, $\theta$ , and $\Delta t$ with $\Delta t = 0.1$ .....	22
2.3	Normalized sideslip distance, $S/Z$ , for a zero-offset trace as a function of dip of the anisotropic overburden, $\theta$ , and the difference between $\theta$ and $\Delta t$ with $\Delta t = 0.1$ . ....	22
2.4	Lateral shift of reflection point with offset for a horizontal reflector beneath anisotropic strata dipping at (a) $45^\circ$ and (b) $15^\circ$ . Distance units are metres. ....	24
2.5	Parametric plot of normalized reflection-point smear versus average normalized sideslip with the dip of the anisotropic overburden varying between $0^\circ$ and $90^\circ$ . .	25
2.6	Interactive model-building display with dip picks applied to several layers. ....	27
2.7	Source traveltimes curves for physical-model dataset. Traveltimes curves are separated by 10 ms and the bold curves are separated by 100 ms. The red segment represents a phase-velocity vector, yellow is the corresponding sideslip vector, and green is the group velocity vector. ....	28
2.8	Source traveltimes curves illustrating Huygen's Principle across a boundary with changing dip. Dip markers are shown in gray. Blue wavefront curves superimpose to make the next traveltimes curve. The inset shows the phase velocity (red), sideslip (yellow) vectors, and group velocity (green) vector, which, divided by the time increment, yields a point on the next wavefront. ....	29
2.9	(a) Physical model from Isaac and Lawton (1999), (b) isotropic depth migration and (c) anisotropic depth migration of physical-model seismic data. Migrated image gathers are overlaid with offset increasing to the right. ....	30
3.1	Interpreting dip from the seismic section. The white lines on the section are velocity-model zone boundaries. The dip may vary laterally within a zone as shown here. The upper section contains the shale-dominated clastic sequence, and the lower section contains carbonates that are assumed isotropic in the velocity model. ....	34





3.2	(a) Image-gather displays for the isotropic model, offset increasing to the right. The black lines represent a straight-line approximation of raytracing to the basement reflector at 6 km depth. (b) Image-gather displays for the anisotropic velocity model. Model parameters $\eta = 0.1$ and $\epsilon = 0.025$ are used for the clastic layers in the upper 2.5 km of the section. ....	36
3.3	Prestack depth migrated sections with varying migration velocity. (a) migrated with the base velocity function scaled to 98%, (b) migrated with 100% of the base velocity function and (c) migrated with the velocity scaled to 102% of the base velocity function. ....	38
3.4	Prestack depth migrated sections migrated with varying values for $\epsilon$ ( $\eta=0$ ). (a) migrated with the isotropic case where $\epsilon=0$ , (b) migrated with $\epsilon=8\%$ and (c) migrated with $\epsilon=16\%$ . Note changes in reflector continuity and in lateral position of the target reflector on the left of the section at 950 ms. ....	40
3.5	Prestack depth migrated sections migrated with varying $\eta$ and $\epsilon=0.08$ . (a) migrated with the isotropic case where $\epsilon=0$ , (b) migrated with $\epsilon=8\%$ and (c) migrated with $\epsilon=16\%$ . Note the change in reflector continuity with negligible change in lateral position of the target events. ....	41
3.6	(a) common-offset image gather and (b) dip-oriented-offset image gather from the anisotropic step model. Note that the migration operator noise creates a checkerboard pattern obscuring upper reflectors on the common-offset image gather in (a) and the migration operator noise is coherent out to the far offsets on the gather in (b). ....	42
3.7	(a) region of depth-migrated stack showing location of (b) the dip-oriented-offset image gather. Seismic events inside dashed ellipses on the gather in (b) correspond with the dipping seismic events on the stack marked with dashed lines in (a). (c) shows the same gather in the common-offset domain. ....	44
3.8	Prestack migrated section using the dip-oriented-offset method (a) with no mute applied to the gathers before stack and (b) with mute applied to the gathers before stack. The boxes highlight linear noise trains that are removed after mute is applied. ....	45
4.1	Depth migrated sections with (a) isotropic and (b) anisotropic migrations. Boxes outline some key differences in imaging. ....	50
4.2	Velocity maps for (a) time migration, (b) isotropic depth migration, and (c) anisotropic depth migration as applied to the Triangle Zone dataset. ....	52



4.3	(a) Prestack time migration, (b) isotropic depth migration, and (c) anisotropic depth migration displayed in time for the Triangle Zone dataset. ....	54
4.4	Correlation between well depth and seismic depth for (a) isotropic depth migration and (b) anisotropic depth migration. The red marker is the well depth that correlates to the seismic event traced in green. ....	55
4.5	Poststack time migration of the Response data set showing Nordegg reflector and proposed location for Well B. ....	57
4.6	Prestack time migration of the Response data set showing well trajectories for Well A and Well B. ....	57
4.7	Prestack depth migration displayed in time with well trajectories. ....	58
4.8	Prestack anisotropic depth migration displayed in time showing well trajectories for Well A and Well B and the sidetrack of Well B. ....	58



## Chapter 1

# Introduction

The problem of seismic imaging below dipping anisotropic strata requires integration of two fields of study: seismic anisotropy and seismic depth migration. This chapter provides an overview of specific aspects and terminologies of these two subjects as they apply to this study. It also provides a summary of the thesis objectives.

## 1.1 Seismic velocity anisotropy

Seismic velocity anisotropy is the dependence of seismic velocity on the direction of wave propagation. A medium that displays this directional dependence is referred to as a seismically anisotropic medium.

One effect of seismic anisotropy is the polarization and separation of orthogonally polarized shear waves, a phenomenon called shear-wave splitting or birefringence. In isotropic elastic media, where the seismic velocity does not change with direction, there are two types of body waves, longitudinal or compressional waves (P) and transverse or shear waves (S), characterized by directions of oscillatory particle motion, or polarization., of the waves: longitudinal and perpendicular to the direction of wave propagation, respectively. In anisotropic media, the polarizations are not, in general, longitudinal or perpendicular to the direction of wave propagation and the shear wave will split into two quasi-shear (qS) waves with quasi-orthogonal polarizations that will, in general, propagate at different velocities. The three waves that propagate through an anisotropic medium are called qP, qS1, and qS2, referring to the quasi-compressional or quasi-P wave and the fast and slow quasi-shear or quasi-S waves, respectively. For further background on anisotropic wave propagation, see Musgrave (1970) and Shuvalov (1981).

Most seismic data acquired for resource exploration in thrust-belt environments are P-wave seismic data. This study focuses exclusively on qP seismic wave phenomena and the imaging of conventional P-wave seismic data.

There are a variety of causes for seismic anisotropy, including aligned fractures, crystal structure, and the regional stress system. In this thesis, I focus on seismic anisotropy caused by layering of sedimentary rocks. Clastic sediments, particularly shales, typically exhibit a symmetry class characterized as transverse isotropy (TI) (Thomsen, 1986), which was defined by Love (1944) to be synonymous with hexagonal symmetry. The qP-wave seismic velocity is constant in all directions parallel to bedding and typically slower in all other directions. A TI medium has one infinite-fold symmetry axis, which is assumed to be normal to bedding in clastic sedimentary rocks. This infinite-fold symmetry axis is hereafter referred to simply as the axis of symmetry. All planes that contain this axis of symmetry are symmetry planes and therefore observations in these planes may be treated in two-dimensions (2D).

Figure 1.1 illustrates the anisotropic velocity symmetry class called TI. The particular case in this figure is referred to as VTI or vertical transverse isotropy because the axis of symmetry is vertical. In the case of interbedded sandstones and shales, the symmetry axis is assumed to be the bedding-plane normal. In all directions parallel to bedding, the velocity is the same, and velocity decreases as the angle of wave propagation approaches the direction normal to bedding.

Seismic imaging of structures below dipping anisotropic strata, where we have a symmetry axis of arbitrary tilt (Figure 1.2), is the focus of this study. We have the similar velocity configuration as in Figure 1.1, with constant seismic velocities in all directions parallel to bedding, but the bedding has arbitrary dip. I propose that dipping anisotropic strata in the

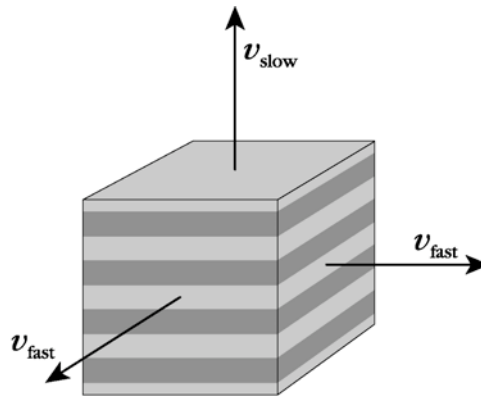


Figure 1.1 Transversely isotropic (TI) medium with a vertical axis of symmetry. The seismic velocity is equal in all directions parallel to bedding and lower perpendicular to bedding.

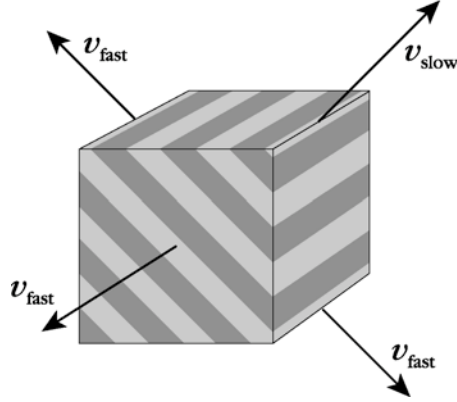


Figure 1.2 A TTI medium is a TI medium with a symmetry axis of arbitrary tilt.

overburden cause positioning errors on seismic reflectors below if velocity isotropy is assumed during data processing and imaging.

Thomsen (1986) defines a simple and useful method for parameterizing a TI medium. Considering only compressional- or P-wave propagation, Equation (1.1) gives the phase velocity magnitude,  $v$ , as a function of phase angle,  $\theta$ , measured from the symmetry axis or bedding-plane normal:

$$v(\theta) = v_0 \sqrt{(1 + \epsilon \sin^2 \theta + D(\theta))}, \quad 1.1$$

where  $v_0$  is the velocity normal to bedding.  $D$  is given here as a function of  $\theta$ , a parameter that has the greatest effect at angles near the symmetry axis,  $\epsilon$  the fractional difference between the velocities parallel and perpendicular to bedding, and  $v_b$ , the shear-wave velocity along the symmetry axis:

$$D(\theta) = \frac{1}{2} \epsilon \left( \frac{v_b^2}{v_0^2} \right) + \frac{4(2\epsilon \gamma \delta)}{(1 - \epsilon v_b^2/v_0^2)} \sin^2 \theta \cos^2 \theta + \frac{4(1 - \epsilon v_b^2/v_0^2 + \gamma \delta)}{(1 - \epsilon v_b^2/v_0^2)^2} \sin^4 \theta \left( \frac{v_b^2}{v_0^2} \right)^{1/2} \quad 1.1a$$

In the weak-anisotropy case, where  $\epsilon$  and  $\gamma$  are both less than 0.25, the compressional-wave velocity is independent of the shear-waves velocity, i.e., the compressional velocity,  $v$ , is independent of  $v_b$ . Thomsen (1986) gives the weak-anisotropy approximation in terms of the parameters  $\epsilon$  and  $\gamma$ :

$$v(\theta) = v_0(1 + \epsilon \sin^2 \theta \cos^2 \theta + \delta \sin^4 \theta). \quad 1.2$$

A significant advantage of the weak-anisotropy equation (1.2) is that the compressional velocity is nearly independent of the shear-wave velocity. In pure vertical-component seismic acquisition, we do not typically have shear-wave velocity information, so I employed Thomsen's weak approximation and the resulting three-parameter formulation, which describes velocity variation with direction using  $v_0$ ,  $\epsilon$  and  $\delta$  in the raytracing for anisotropic depth migration, as described in Chapter 2. In this formulation, the relationships between velocity and each of  $\epsilon$  and  $\delta$  can be written in a simple, intuitive form, where,

$$\epsilon = \frac{C_{11} - C_{33}}{2C_{33}} = \frac{v(90^\circ) - v(0^\circ)}{v(0^\circ)}, \quad 1.2a$$

and

$$\delta = \frac{(C_{13} + C_{44})^2 - (C_{33} - C_{44})^2}{2C_{33}(C_{33} - C_{44})} = 4 \frac{v(45^\circ) - v(0^\circ)}{v(0^\circ)}. \quad 1.2b$$

The phase velocity,  $\bar{v}$ , is the velocity of wave propagation normal to the wavefront and the group velocity,  $\bar{g}$ , is the velocity of energy transport away from the energy source. This relationship between phase and group velocity is shown in equations (1.3) and (1.4) as given by many authors (e.g., Postma, 1955; Brown et al., 1991). The relationship between the magnitudes of the phase and group velocity vectors is:

$$g^2 = v^2 + \left( \frac{\partial v}{\partial \theta} \right)^2. \quad 1.3$$

The relationship between the angles of the two vectors relative to the symmetry axis (i.e., normal to bedding) is:

$$\theta = \theta_0 + \arctan \frac{\partial v / \partial \theta}{v}, \quad 1.4$$

where  $\theta$  is the angle between the group velocity vector and the symmetry axis and  $\theta_0$  is the



angle between the phase-velocity vector and the symmetry axis.

## 1.2 Seismic migration

The goal of seismic depth migration is to invert the reflections recorded in time for the reflectors in depth. The process is called “migration” because seismic reflection events are “migrated” to the correct lateral reflector position. Anisotropic depth migration is a specific type of migration that corrects for seismic anisotropy. To put the anisotropy problem into a seismic-migration context, the following three sections and their associated figures illustrate the differences between time migration, depth migration, and anisotropic depth migration.

Each illustration used in the following four sections shows an aplanatic surface, which is the locus of possible reflection locations for a given reflection time. Since we do not know where in the subsurface the seismic reflection came from, Kirchhoff migration takes the reflected energy and copies it to all points along the aplanatic surface, creating a Kirchhoff migration operator. Once this process is repeated for all reflection energy in the seismic data volume, the energy along the migration operator constructively adds up at reflector locations and destructively cancels where reflectors are absent. For a thorough discussion on Kirchhoff migration, see Chapter 4 of Seismic Data Processing by Yilmaz (1987).

### 1.2.1 Time migration

Sheriff (1991) defines time migration as, “migration in which some approximation is made to the wave equation or the handling of velocities ... such that the image is not a true depth migration.” Typically, Kirchhoff time migration employs a straight-ray approximation that assumes a laterally homogeneous, isotropic subsurface. Figure 1.8 shows an aplanatic surface under the assumption of time migration. Time migration allows vertical velocity heterogeneity but minimal lateral velocity heterogeneity. Note in Figure 1.8 that the rays from source to reflection point and back to the receiver are straight and therefore the aplanatic surface is a smooth ellipse. Time migration is robust, but does not, in its most basic form, correct for lateral velocity variations or anisotropy in the subsurface.

### 1.2.2 Depth migration

Depth migration deals correctly with lateral and vertical velocity changes in the subsurface. The aplanatic surface in Figure 1.9 illustrates how depth migration corrects for lateral

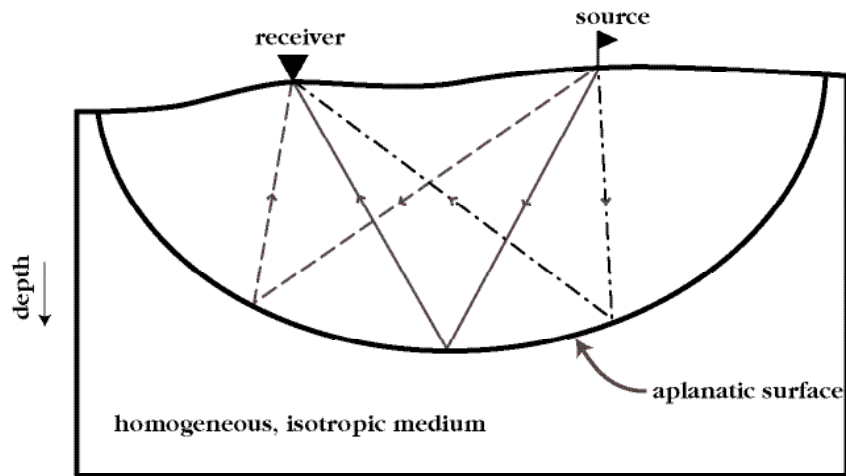


Figure 1.3 Aplanatic surface for a time migration assuming homogeneous, isotropic media

velocity heterogeneity. By raytracing through a velocity model, one can calculate traveltimes for all reflector locations for a given reflection time when high- or low-velocity regions are present in the subsurface. Note the kink in both the ray and the aplanatic surface corresponding with the edge of the high velocity medium. The ray bending at the interface between high and low velocities in this example is dependent on the ratio of the two velocities and orientation of the boundary between them, according to Snell's Law. Depth migration's dependence on an accurate velocity model makes it less robust than time migration, but it has the ability to properly position subsurface structures in the presence of lateral velocity heterogeneity.

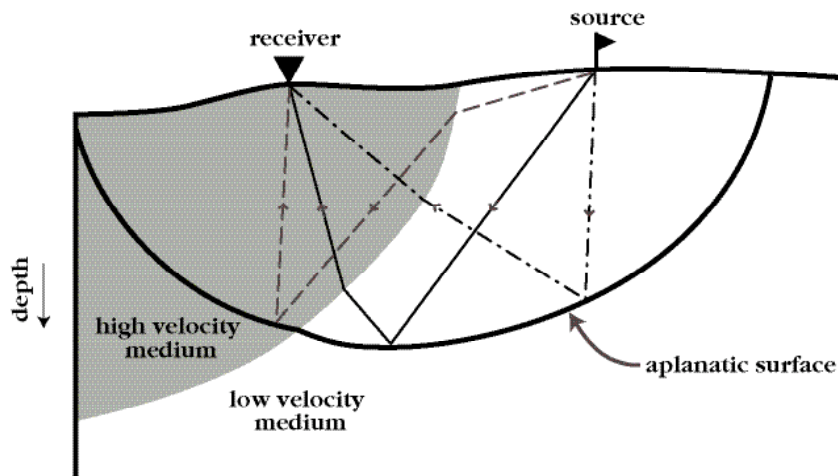


Figure 1.4 Aplanatic surface for a traditional depth migration that corrects for lateral velocity heterogeneity but assumes velocity isotropy.

### 1.2.3 Anisotropic depth migration

Anisotropic depth migration is similar to isotropic depth migration, but it also corrects for imaging and positioning errors caused by the sideslip of seismic energy as it passes through dipping anisotropic strata. Figure 1.5 shows an aplanatic surface in a TTI medium. The skewed shape of the surface results from the higher seismic velocity in the bedding-parallel direction and a slower velocity in the bedding-normal direction. The skewed shape of this aplanatic surface corrects for the sideslip effect discussed in section 1.1.

In a thrust-belt environment, both lateral velocity variations and dipping anisotropic media are present. The most accurate depth migration in a thrust-belt environment will then correct for both ray bending and sideslip, as illustrated by figure 1.6.

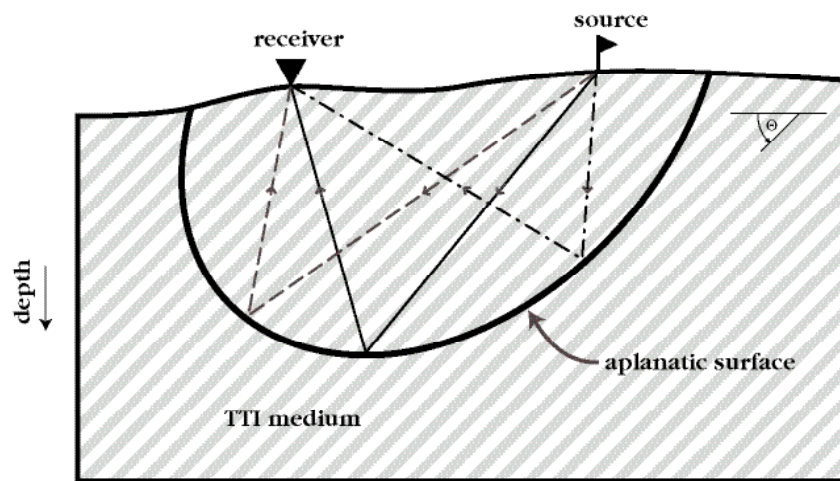


Figure 1.5 Aplanatic surface for an anisotropic depth migration that corrects for velocity anisotropy. The skewed shape of the surface corrects for the sideslip effect. Dip is shown by  $\theta$ .

### 1.2.4 Migration velocity analysis

An accurate migration requires accurate input seismic velocities. Zhu et al. (1998) provide a theoretical basis for migration velocity analysis in a tutorial paper. These authors and others (e.g., Yilmaz 1987; Schultz and Canales 1997) describe established methodologies in migration velocity analysis.

One fundamental velocity diagnostic involves inspection of prestack image gathers. A prestack image gather is a collection of seismic traces from a single imaging point; each trace

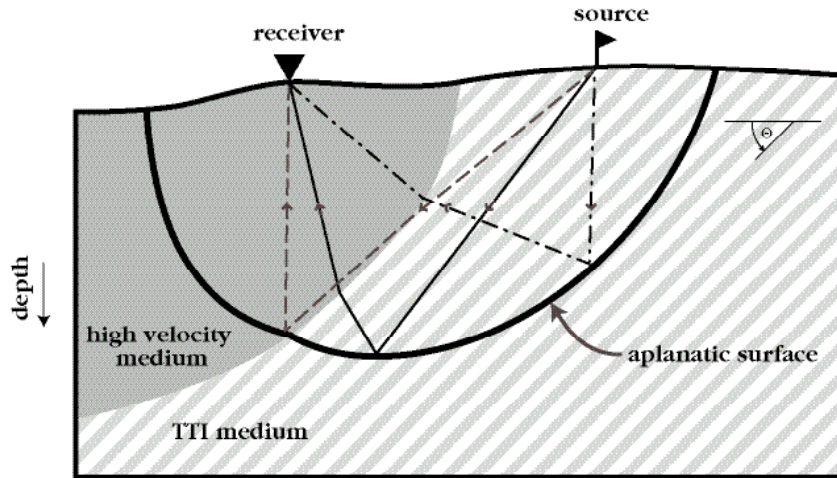


Figure 1.6 Aplanatic surface for an anisotropic depth migration that corrects for both raybending caused by lateral velocity changes and sideslip caused by seismic anisotropy.

in the gather has a different source-receiver offset (the distance from seismic source to receiver). If the migration velocity is too low, a reflector at a certain time will be positioned too shallow on the depth-migrated output. A reflector imaged at a far offset has a longer reflection time than for a near offset, so the depth error on far offsets will be larger than the depth error on near offsets, i.e., the reflector will appear shallower at far offsets than at near offsets. If the migration velocity is too high, then the reflectors will be too deep and, again, the depth error will increase with offset, so the reflector will appear deeper at far offsets than at near offsets. The dependency of reflector depth on offset is used as a velocity diagnostic, as described by Zhu et al. (1998) and illustrated in Figure 1.7. When the input seismic

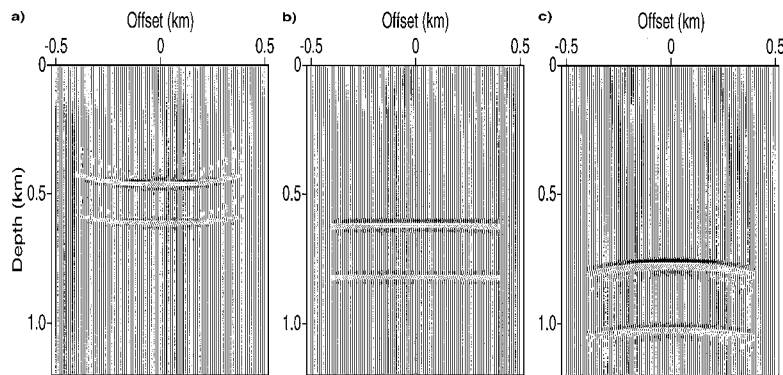


Figure 1.7 Prestack migrated image gathers after Zhu et al. (1998). (a) was migrated with too low an input velocity, (c) was migrated with too high an input velocity, and (b) was migrated with the correct input velocity.

velocity is too low (Figure 1.7a) the seismic event turns upward, showing decreasing depth with increasing offset, and if the input velocity is too high (Figure 1.7c), the event turns downward, showing increasing depth with increasing offset. Accurate input velocities will place the seismic event at the same depth independent of the source-receiver offset. We will then observe a flat seismic event on the prestack gather (Figure 1.7b).

### 1.3 History of anisotropic migration research

For decades, geophysical research has addressed seismic imaging problems caused by seismic velocity anisotropy. However, only in recent years has the full extent of the problem of imaging geologic structures on seismic below dipping anisotropic media been understood. This understanding underscores the need for a practical seismic-imaging methodology that corrects for seismic anisotropy in depth migration of surface seismic data in regions of complex structural geology. Current research into imaging and position errors caused by seismic anisotropy documents and corrects for sideslip on seismic images. An understanding of the sideslip phenomenon and its effect on seismic data has developed over several decades of research into anisotropic wave propagation and seismic imaging.

The history of development of anisotropic seismic imaging to date can be divided into three overlapping phases of discovery and development. Initially, studies into the theory of elastic wave propagation and corresponding experimental laboratory data revealed wave-propagation phenomena that pose significant problems with the positioning of structures on seismic images. The full impact of anisotropic wave propagation on structural positioning was not fully understood nor corrected for decades.

The next phase is the algorithm-design phase. The literature shows the development of several algorithms employing various simplifying assumptions as the availability of computing power increased. Practical migration researchers blamed anisotropy for unresolvable imaging problems during this phase.

The current phase of development combines the theoretical and field-measurement observations with anisotropic imaging algorithms to develop a practical solution to the anisotropic imaging problem. The objective of the practical-solution phase is to find practical seismic-imaging methodologies that apply to various anisotropic imaging problems

worldwide.

### 1.3.1 Problem definition

A major anisotropy problem in seismic imaging that is the focus of this thesis is the lateral-positioning error on subsurface targets, as detailed above in section 1.1. Recent work shows this effect in the context of hydrocarbon exploration (Isaac and Lawton, 1999), but studies into crystallography illustrated this phenomenon as early as the 1950s (Markam, 1957; Musgrave, 1959).

A significant contributor to the anisotropic lateral-position error is the difference between the velocity of energy transport, the group or ray velocity, and the velocity of the wave in the direction normal to the wavefront, the phase velocity. As described above, the group and phase velocities are not, in general, equal due to the angular dispersion of velocities in an anisotropic medium (Dellinger and Vernick, 1994) and the difference between these two vectors gives us the lateral positioning error or sideslip error (Isaac and Lawton, 1999; Vestrum et al., 1999).

Experimentally, Markam (1957) and Musgrave (1959) observed the lateral displacement of elastic-wave energy using the ultrasonic pulse method. Figure 1.8 shows the path of reflected elastic-wave energy across an anisotropic crystal (Musgrave, 1959). The plane-wave segment generated from the source transducer at the top of the sample reaches the horizontal reflector below at normal incidence with respect to the phase velocity. Snell's law dictates that, for phase-velocity vectors, the angle of incidence is equal to the angle of reflection for the same wave phase, and therefore the reflected energy returns to the source after imaging the reflector at a position laterally displaced from the source position.

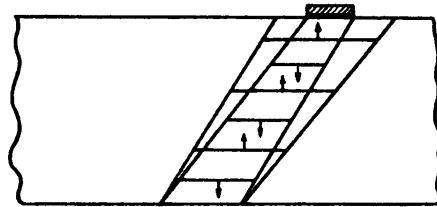


Figure 1.8 Reflection back and forth oblique to the wave normal defined by perpendicular distance (after Musgrave, 1959).

Researchers studying elastic waves in anisotropic crystals demonstrated the lateral movement or sideslip of elastic wave energy in the 1950s. In that same time period, Hagedoorn (1954) introduced concepts of seismic migration to the geophysical community. However, it was still 20 years before major research into seismic imaging would be completed (for example: Stolt, 1978; Schultz and Sherwood, 1980). There appears to have been no attempt to document or correct lateral position errors on field seismic data during this time period. As outlined in the next section, it was the late 1980s before seismologists began developing algorithms to correct for anisotropy in seismic imaging.

### 1.3.2 Algorithm design

The completion of much of the theoretical groundwork for anisotropic migration happened in the algorithm-design phase. Parameterization schemes were defined and algorithms using various assumptions developed. Petrophysical studies during this period (Thomsen, 1986; Vernik and Liu, 1997) further described the need for anisotropic corrections in seismic data processing.

Thomsen (1986) offered practical and convenient parameters to describe the velocity behaviour in a transversely isotropic medium and a significant table of values of anisotropic parameters of rocks. Thomsen's parameterization scheme and database of field samples prompted further practical work in correcting for anisotropy on seismic images.

Initially, migration researchers used the assumption of VTI, where the symmetry axis or bedding-plane normal is vertical. This assumption was first used in the study of nonhyperbolic moveout (Hake et al., 1984; Thomsen and Tsvankin, 1994) and then employed in seismic migration. Uren et al. (1990), were early publishers of migration results using an algorithm that corrects for homogeneous VTI media in the overburden. They used a frequency-domain migration to obtain an accurate image of anisotropic physical-model seismic data. Other implementations of VTI migrations include 2D depth migration algorithms by Uzcategui (1995), Phadke et al. (1994), Sena and Toksöz (1993), and Alkhalifah's (1995) Gaussian beam migration.

Early work into algorithm development also included investigation into raytracing algorithms to solve for traveltimes calculated using a model containing anisotropic velocities. Ha (1986) developed an anisotropic wave-propagation algorithm to investigate the differences in

synthetic seismograms between a periodically layered medium and an equivalent TI medium. Gibson et al. (1991) offered a 3D paraxial raytracing solution that calculates traveltimes and amplitudes in heterogeneous, anisotropic media. The examples in the work of Gibson et al. (1991) are in generating synthetic seismograms, but the authors correctly point out that the efficiency of paraxial raytracing makes it well suited for the calculation of Kirchhoff migration traveltimes.

Larner and Cohen (1993) and Alkhalifah and Larner (1994) investigated position errors on migrated images caused by the presence of TI media in the overburden. Alkhalifah and Larner (1994) showed a good numerical example of the lateral-positioning error caused by TTI media in the overburden, perhaps the first example of a migration paper showing this sideslip error on seismic data. Figure 1.9 shows time-migrated images of numerical seismic data from Alkhalifah and Larner (1994). The lateral positioning error on the migrated image of horizontal reflectors in Figure 1.9b, where the anisotropic model has a tilted axis of symmetry, is over 200 m for the reflector at 2.2 seconds. This example clearly shows the need for anisotropic correction when TTI media are present in the overburden.

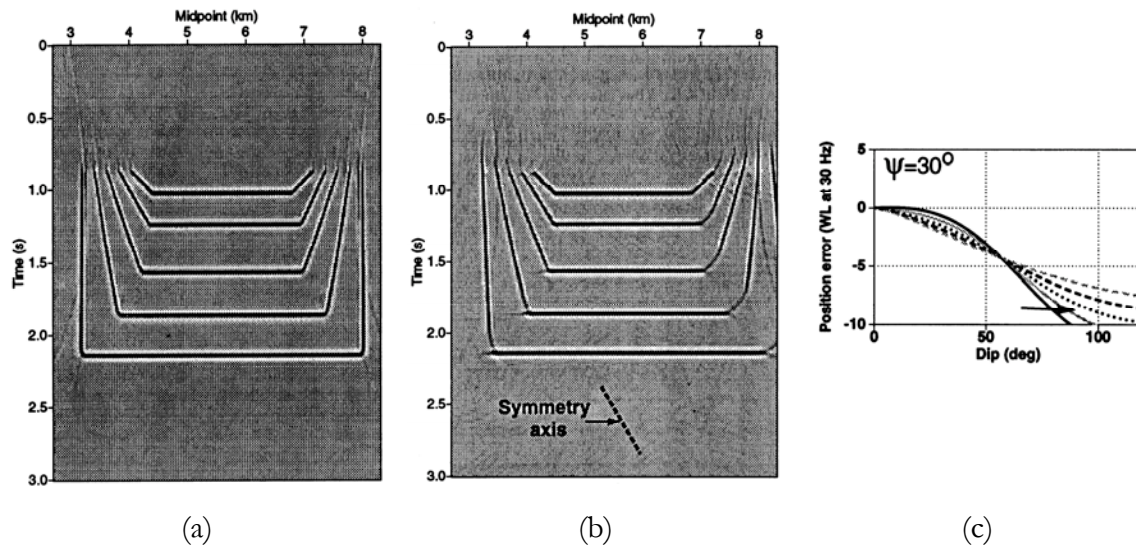


Figure 1.9 Isotropic time migrations of numerical-model seismic data from Alkhalifah and Larner (1994). (a) has an isotropic model and (b) uses an anisotropic model with  $\eta = 0.11$ ,  $\epsilon = -0.035$ , and a  $30^\circ$  tilted symmetry axis. Note the lateral position change between (a) and (b) of the horizontal reflectors. (c) shows a graph of positioning error versus reflector dip with a tilt of the anisotropic symmetry axis,  $\psi$ , of  $30^\circ$  (after Alkhalifah and Larner, 1994).



The work of Alkhalifah and Larner (1994) also illustrates the lack of understanding of the sideslip problem in the migration-research community at that time. Another of their figures (shown in Figure 1.9c) contains curves of position error versus reflector dip. The figure shows that the position error was predicted to be zero when the reflector dip is zero, for a symmetry axis tilted at  $30^\circ$ . Traditional geophysics folklore dictated that horizontal reflections do not move laterally after migration. Perhaps Alkhalifah and Larner (1994) and their reviewers did not observe this position-error discrepancy between the figures because the lateral-position error on horizontal reflectors was not yet completely understood by migration researchers.

Although the tools were established for raytracing and imaging in the anisotropic case, the papers mentioned in this section include only numerical or physical-model seismic data. Each paper also points to the improvement in accuracy of imaging and/or seismic traveltimes when raytracing and imaging includes anisotropic velocities.

In the next section, I will deal with the practical exploration problems caused by seismic-wave sideslip in anisotropic media and the current attempts to address these problems.

### 1.3.3 Practical applications

In 1995, Ball published a thorough case study of 3D anisotropic depth migration (ADM) from offshore Zaire (Ball, 1995). Integrating offset VSP and ultrasonic core-sample measurements to obtain values for his anisotropic velocity model, he showed the extent of anisotropy in the sediments in this area. Values in his anisotropic velocity model for  $\epsilon$  ranged from 0.15 to 0.22 in the clastic overburden.

Ball's migration algorithm is a Kirchhoff depth migration using anisotropic traveltimes. The anisotropic finite-difference traveltimes generator calculates surfaces of constant time. The wave surfaces move forward each time step through the model using the phase velocity. The author observed unexplained inaccuracies when using the anisotropic traveltimes calculator that may result from using the phase velocities rather than group velocities to propagate the wave surfaces.

Practical migration researchers discussed seismic anisotropy as an unresolved imaging issue (e.g., Lines et al., 1996; Gray, 1997). Schultz and Canales (1997) observed the anisotropy

problem in velocity model building where seismic velocities are greater than near-vertical velocities measured in wells. Their anisotropy correction was documented as a vertical scaling to the seismic depth image to make the seismic depth section tie the well depths.

Isaac and Lawton (1999) use similar laboratory methodology to that of Musgrave (1959), showing the lateral-positioning error caused by the presence of TTI media. The fundamental difference between Musgrave on the one hand and Isaac and Lawton on the other was the application of their research. Whereas Musgrave studied the physics of crystals, Isaac and Lawton (1999) focussed on seismic imaging problems in a thrust-belt environment.

Figure 1.10 shows the migrated seismogram from an ultrasonic pulse transmission experiment (Isaac and Lawton, 1999) with a configuration similar to the experiment in Figure 1.8. They show the same result reported by Markam (1957) and Musgrave (1959). The energy from the ultrasonic pulse on the other side of the sample is laterally shifted from the source. When illustrating the application of the sideslip effect to seismic data, Isaac and Lawton performed an ultrasonic pulse reflection experiment designed as a scaled surface-seismic experiment.

The significance of the sideslip effect on surface-seismic data is clearly illustrated in Figure 1.11. Figure 1.11a is a cross section of a scaled physical model used to acquire the physical-model seismic data shown in Figure 1.11b. The reflection from the vertical structure beneath the dipping anisotropic strata is laterally mispositioned by a scaled distance of 290 m. Isaac

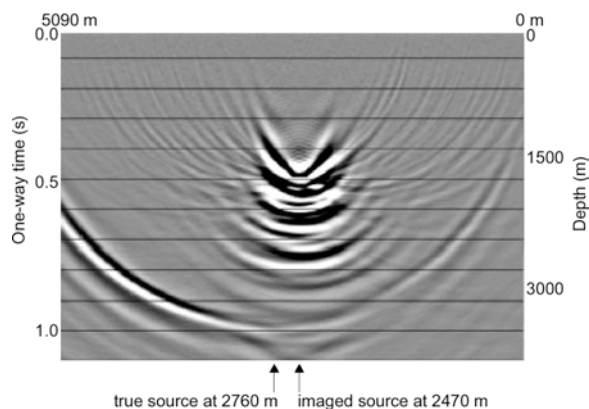


Figure 1.10 Migrated image of ultrasonic-pulse transmission experiment (after Isaac and Lawton, 1999). Distance measurements are scaled 1:10000 from the laboratory setup.

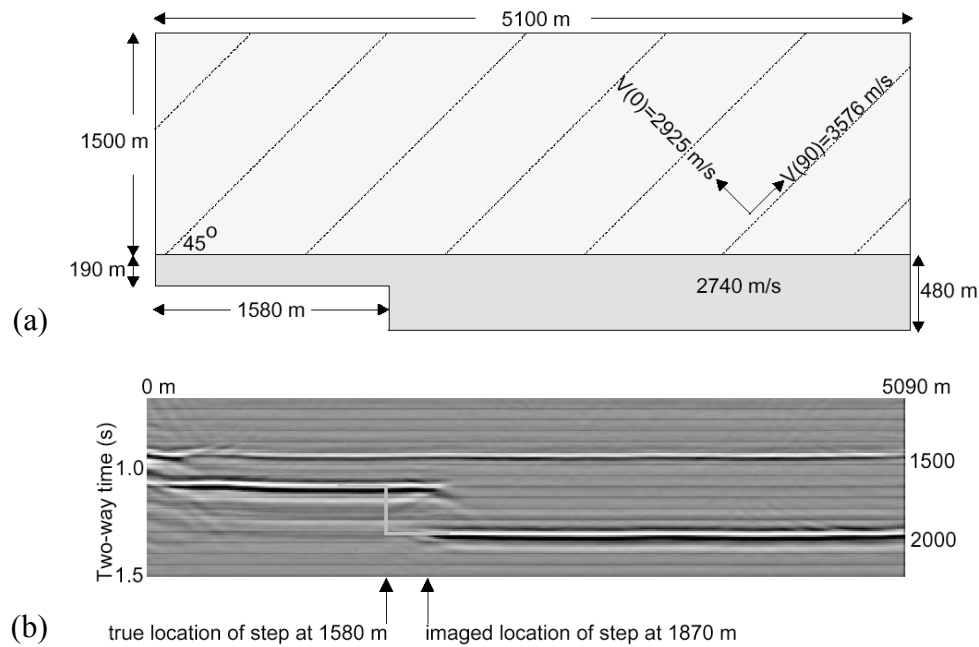


Figure 1.11 (a) Anisotropic physical model and (b) corresponding time-migrated seismic section. Note the lateral position error on the seismic image of 290 m resulting from the sideslip effect (after Isaac and Lawton, 1999).

and Lawton (1999) illustrated with these physical-model experiments that the sideslip effect causes major position errors on seismic images when dipping anisotropic strata are present in the overburden and only isotropic velocities are used in the migration.

The new understanding of the implications of sideslip on seismic imaging resulted in several papers on the subject. Di Nicola-Carena (1997) illustrated the sideslip error when migrating numerical-model seismic data with isotropic and anisotropic algorithms. In 1998, the Canadian Society of Exploration Geophysicists dedicated an entire session of papers at the annual convention to anisotropic migration (Vestrum, et al., 1998; Leslie and Lawton, 1998; Ferguson and Margrave, 1998; Schmid et al., 1998; Dai et al., 1998; Fei et al., 1998), all of which deal with dipping TI media. In contrast, the previous year had only one paper on anisotropic migration (Vestrum and Muenzer, 1997) and one paper on field measurements of anisotropic parameters of shales (Leslie et al., 1997). Even though several publications describe possible anisotropic depth-migration algorithms, the practical implications of lateral mispositioning on seismic images brought a publication boom on anisotropic migration and an active interest in the topic by seismic processing contractors.

The motivation for this thesis rose from the understanding of the practical implications of the sideslip error on imaging structures below dipping anisotropic strata. The author published an example of anisotropic depth migration (Vestrum and Muenzer, 1997) at the commencement of this work and began developing an anisotropic-depth-migration algorithm and model-building methodology to quantify and correct for the lateral-position error on exploration seismic data. Educating the resource exploration community of the problems of imaging below dipping anisotropic strata and publishing case histories on the imaging improvements with proper application of ADM through the course of this work (Vestrum and Muenzer, 1997; Vestrum, et al., 1998a; Vestrum, et al., 1998b; Vestrum and Lawton, 1999; Vestrum and Lawton, 2000; Vestrum et al., 2001; Vestrum, 2001; Vestrum, 2002, Vestrum et al., 2003) contributed to the current widespread use of ADM to reduce exploration risk in complex-structured resource exploration.

#### **1.3.4 Conclusions from the historical account**

The practical application of imaging and positioning problems caused by seismic anisotropy in a thrust-belt environment has led to a recent increase in research into anisotropic imaging. The sideslip effect and its potential to misposition subsurface exploration targets by several hundred metres on seismic images has fuelled this research.

The sideslip effect was well documented over 40 years ago in laboratory studies of elastically anisotropic crystals. This was long before the development of high-resolution surface seismic and depth migration. The link between sideslip and structural mispositioning was not documented at that time but is demonstrated in this thesis.

Research advancements in seismic imaging and the development of algorithms for raytracing and migration in the presence of anisotropic media have made anisotropic depth migration possible. Documentation of the role of sideslip in lateral mispositioning of subsurface targets yielded a practical resource-exploration problem for ADM to solve.

The application of ADM to lateral mispositioning problems is a recent focus of geophysical research, but development of the theory and technology developed over several decades. This focus of this thesis is on the application of ADM to foothills datasets to reduce oil-and-gas exploration risk.

## 1.4 Structure of thesis

The approach to the problem of imaging structures below anisotropic strata follows the historical context and technical understanding outlined in this chapter. Using an understanding of seismic depth-migration and anisotropy theory, the goals of this research are to develop an anisotropic depth migration algorithm and methodology, demonstrate its effectiveness at correcting for imaging and positioning problems on seismic data, and apply this technology in reducing oil-and-gas exploration risk.

Chapter 2 discusses the anisotropic depth-imaging algorithm developed for this thesis. The assumptions of bedding dip orientation, anisotropic symmetry, and velocity heterogeneity are also described. To test the algorithm, I attempt to resolve the seismic imaging problem in the physical-model dataset from Isaac and Lawton (1999) as shown in Figure 1.11.

One cannot perform seismic migration without an accurate model of subsurface seismic velocities. Chapter 3 describes methodologies for estimating and updating velocity models that include sufficient information about anisotropy and bedding dip to honour the assumptions outlined in Chapter 2.

Employing assumptions from Chapter 2 and velocity-model interpretation methodologies from Chapter 3, seismic data from two sample seismic datasets from the Alberta Foothills are processed through to anisotropic depth migration. Chapter 4 discusses the results of these two migrations and details an exploration case history where ADM was employed. Each of these seismic examples shows imaging and positioning improvements on field seismic data and correlation to well data when depth migration corrects for seismic anisotropy.

The final case history in Chapter 4 addresses the ultimate purpose of this research: to reduce risk in hydrocarbon exploration. The location for a natural-gas development well was chosen from seismic sections processed using the assumption of isotropic velocities. Drilling off the front of the leading edge of the exploration target revealed the incorrect position of the target structure on these processed seismic data. Anisotropic depth migration was required to position the subsurface structure accurately. The new structural position interpreted on the ADM section led to additional drilling on the structure and a successful well.



## Chapter 2

# Anisotropic depth migration

The anisotropic depth migration algorithm developed and implemented in this study is a 2D migration that corrects for lateral velocity heterogeneity and seismic anisotropy in P-wave data. This chapter details the assumptions made and the specific geologic setting targeted by this algorithm. A migration example using physical-model seismic data illustrates how the algorithm corrects for the sideslip error described in Chapter 1.

The problem addressed by software written for this thesis is imaging below TTI media, as defined in Section 1.2 of Chapter 1. Therefore, this study's algorithmic needs focus incremental development on adding anisotropy corrections to seismic migration. The development platform I chose was the proprietary depth migration and velocity model-building system at Kelman Technologies Inc, a provider of seismic processing services to the Canadian resource exploration community. This company was chosen because it had its own in-house development team and proprietary depth-imaging software focussed on imaging problems in the Canadian thrust-belt.

I took the established depth-imaging software and velocity model-building tools and made modifications as follows: (1) defined additional parameters in the velocity model, (2) modified the model-building software to permit the user to enter these additional parameters into the velocity model, and (3) updated the program that calculates migration traveltimes to read the additional anisotropic parameters and apply corrections to the migration traveltimes for TTI anisotropy.

This chapter details parameter definitions and discusses the inherent assumptions made for the definition of the anisotropic velocity model. The modifications that created the anisotropic depth migration from a traditional isotropic depth migration are also described. Finally, the results of testing this algorithm on physical-model seismic data are presented.

## 2.1 Model definition

The velocity model defined for this study includes the following parameters as employed in equation 1.1:

- $v_0$ : P-wave phase velocity normal to bedding;
- $\delta$ : Thomsen's (1986) delta;
- $\epsilon$ : Thomsen's (1986) epsilon; and
- $\theta$ : bedding dip.

Values for all of these parameters are allowed to vary in depth and vary laterally along the 2D velocity model.

### 2.1.1 The Sideslip Effect

Figure 1.3 illustrates a propagating wavefront in a TI medium with a tilted axis of symmetry. The sideslip velocity,  $\bar{s}$ , is defined by equation 2.1 as the partial differential of the phase velocity,  $v$ , with respect to  $\theta$ . The sideslip velocity is the vector difference between the group and phase velocities and the rate at which energy moves tangential to the wavefront

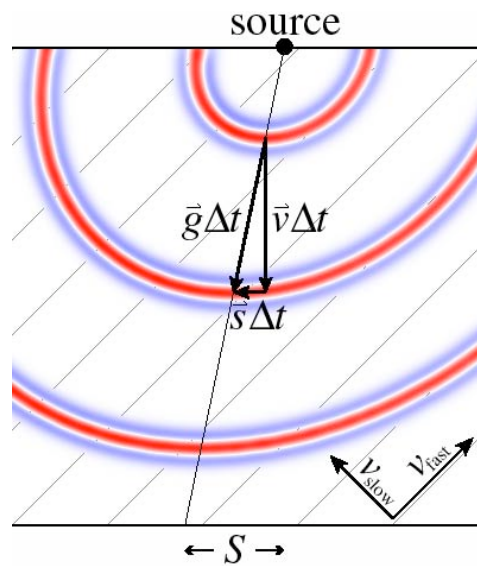


Figure 2.1 Waves propagating across dipping anisotropic strata separated by  $\Delta t$ . The grey lines represent the  $45^\circ$  dip orientation. The lateral distance between the source and the zero-offset reflection point is the zero-offset sideslip distance  $S_0$ .



(Dellinger, 1991). Vector addition of sideslip-velocity and phase-velocity vectors yields the group velocity,  $\bar{g}$ , which is the velocity of energy transport (in a lossless medium). The equation for the sideslip magnitude,  $s$ , is obtained by differentiating Equation 1.2 with respect to  $\theta$ :

$$s \equiv \frac{\partial v}{\partial \theta} = v_0 \left[ 2\theta (\cos^3 \theta \sin \theta - \cos \theta \sin^3 \theta) + 4\theta \cos \theta \sin^3 \theta \right]. \quad 1.5$$

The sideslip distance,  $S$ , is the displacement of a reflection point from the midpoint between seismic source and receiver for a horizontal reflector below a layer of anisotropic strata with a tilted axis of symmetry. If we consider only the zero-offset sideslip distance as a function of the vertical thickness of the dipping anisotropic strata,  $Z$ , and the magnitudes of the sideslip velocity,  $s$ , and phase velocity,  $v$ , we may define the zero-offset sideslip distance,  $S_0$ , as:

$$S_0 \equiv \frac{s}{v} Z. \quad 2.2$$

This equation is valid only for the case of zero-offset distance between the source and receiver. In general throughout this thesis, I refer to the distance between the true position of the reflection point and the reflector position resulting from the assumption of isotropy as the “lateral-position error,” which, in the case of imaging a horizontal reflector below dipping anisotropic strata, is equal to the sideslip distance. The lateral-position error is discussed in detail in the migration section below and in subsequent chapters.

The sideslip distance is dependent on the thickness and dip of the anisotropic overburden as well as the anisotropic parameters,  $\epsilon$  and  $\delta$ , for the overburden media. Figures 2.2 and 2.3 illustrate the dependence of zero-offset sideslip distance on these parameters. In the case of horizontal reflectors below dipping anisotropic strata, the angle between the symmetry axis and the phase velocity direction,  $\theta$ , will be equal to the tilt of the anisotropic symmetry axis,  $\theta$ . (Note that the tilt of the symmetry axis, the angle of the symmetry axis with respect to the vertical, will be equal to the dip of the anisotropic overburden, angle between the horizontal and the bedding plane measured in a vertical plane containing the dip direction. These terms will be used interchangeably in this thesis and represented by  $\theta$ .) Since  $S_0$  dependence on  $Z$  is linear (Equation 1.5), I plot  $S_0/Z$  as a function of  $\theta = \theta$  and the

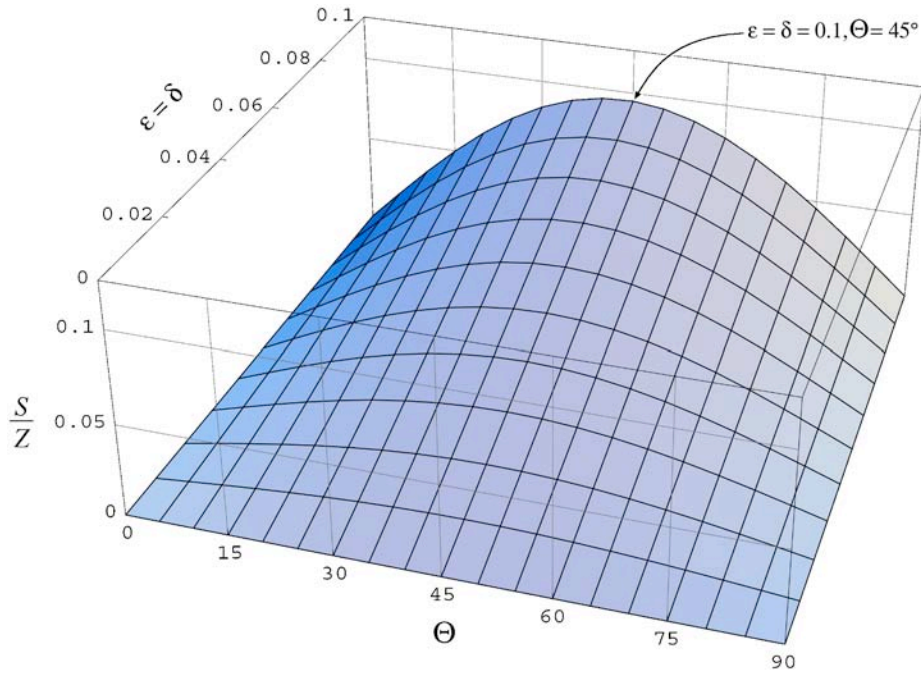


Figure 2.2 Normalized sideslip distance,  $S_0/Z$ , for a zero-offset trace as a function of dip of the anisotropic overburden,  $\epsilon$ , and  $\delta$  with  $\epsilon = \delta$

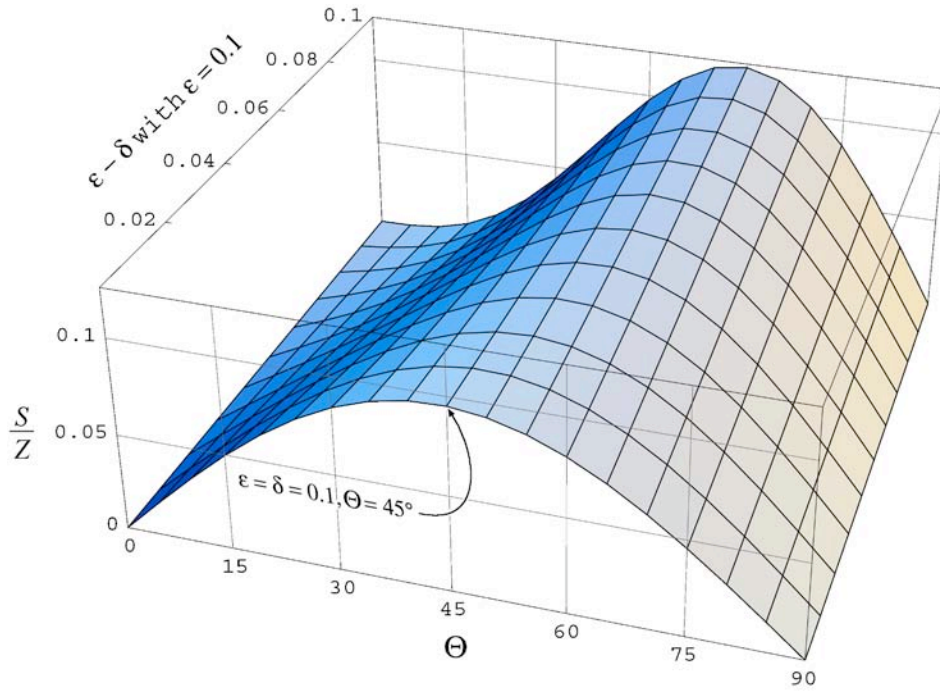


Figure 2.3 Normalized sideslip distance,  $S_0/Z$ , for a zero-offset trace as a function of dip of the anisotropic overburden,  $\epsilon$ , and the difference between  $\epsilon$  and  $\delta$ .  $\epsilon = 0.1$ .

overburden dip,  $\theta$ , in Figure 2.2. Then I hold  $\theta$  constant and plot  $S_0/Z$  as a function of  $\epsilon$  and the difference between  $\epsilon$  and  $\delta$  in Figure 2.3. An example sideslip-error estimation from these surfaces is for a 1000-metre-thick anisotropic stratum dipping  $45^\circ$  and for  $\epsilon = \delta = 0.1$ . From the surface in Figure 2.2 we can see that  $S_0/Z = 0.095$  for these values of  $\epsilon$ ,  $\delta$  and  $\theta$ ; so if we were imaging a horizontal seismic reflector beneath 1000 m of this material, we would expect 95 m of lateral position error in the zero-offset case.

Note that in Figure 2.2 the sideslip error increases with increasing values of the anisotropy parameters and that when  $\epsilon = \delta$  the sideslip error reaches a maximum at  $45^\circ$  dip. In Figure 2.3 observe that, with  $\theta$  fixed, decreasing  $\epsilon$  merely changes the distribution of the sideslip error with respect to dip.

Note that all of the directions in all equations in this section and in models defined for migration in this thesis are parameterized in terms of angle with respect to the symmetry axis, not in terms of angle with respect to the vertical.

### 2.1.2 Offset-dependent sideslip

Figures 2.2 and 2.3 show the sideslip distance for the zero-offset trace, where the source and receiver are at the same location, but seismic acquisition typically includes a range of source-receiver offsets. The question then arises, how does the lateral-position error, or sideslip distance, change with source-receiver offset? To answer this question, a simple raytracer was designed to find the minimum-traveltime raypath from source to reflection point to receiver for the case of a horizontal reflector beneath dipping anisotropic strata, similar to the geometry in Figure 1.3, for any source-receiver combination. I then investigated sideslip dependency on source-receiver offset.

Figure 2.4a shows minimum-traveltime raypaths for offsets ranging from zero to 2000 metres through a 1000-metre-thick TTI medium dipping  $45^\circ$ , with anisotropic parameters  $\epsilon = 0.12$  and  $\delta = 0.03$ . Not only is the reflection point shifted laterally from the midpoint between source and receiver, but each offset images a slightly different location in the subsurface. In this case, the far-offset trace shows less lateral shift from the source-receiver midpoint than the zero-offset trace. The area over which all of the traces image the subsurface is defined as the reflection-point smear,  $S'$  (Figure 2.4a), because all of the traces

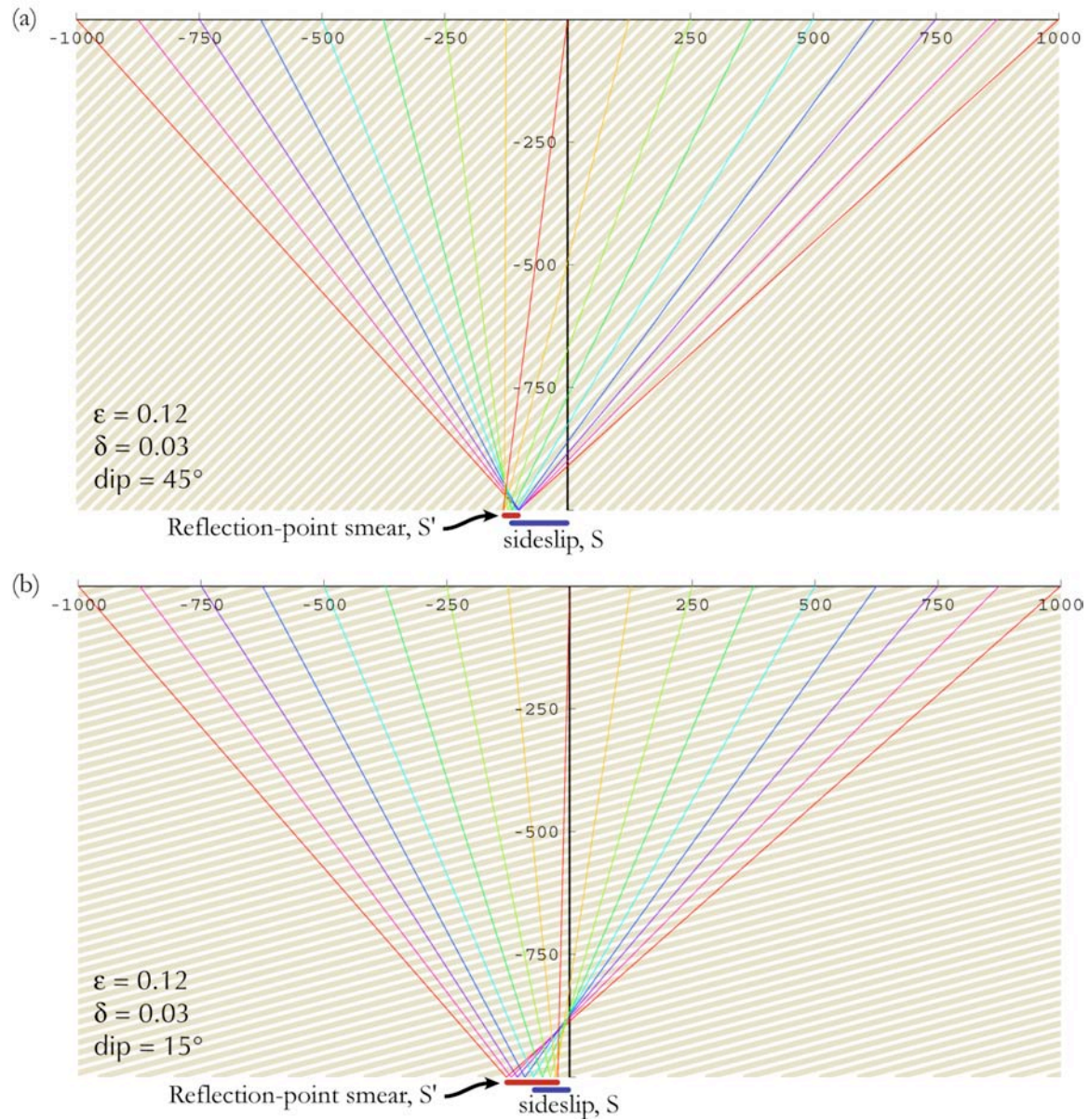


Figure 2.4 Lateral shift of reflection point with offset for a horizontal reflector beneath anisotropic strata dipping at (a)  $45^\circ$  and (b)  $15^\circ$ . Distance units are metres.

are not imaging the same reflection point.

Figure 2.4b shows the same experiment as shown in Figure 2.4a with the overburden dip changed from  $45^\circ$  to  $15^\circ$ . Here there is much less lateral shift at zero offset, as predicted by Figure 2.3, but the lateral shift at the far offset is much larger than the zero-offset sideslip,

giving a larger average lateral shift than Figure 1.5 predicts. Also note that the reflection-point smear in this case is significantly larger than the smear in the  $45^\circ$  case.

In an effort to consider both of these phenomena, namely the sideslip effect and reflection-point smear, Figure 2.5 shows a parametric plot of reflection-point smear ( $S'$ ) versus average sideslip ( $\bar{S}$ ) for dip angles ranging from  $0^\circ$  to  $90^\circ$  for anisotropic parameters  $\epsilon = 0.12$  and  $\delta = 0.03$ . The smear is defined as the distance from the reflection point at zero offset to the reflection point at the maximum offset. This case has the maximum offset equal to twice the reflector depth, as in Figure 2.4, and then normalized by the reflector depth. The value for the average sideslip is simply the mean of the zero offset sideslip distance and the far offset sideslip distance. Again, the far offset is twice the depth to the reflector and the average sideslip is then normalized by the reflector depth. As a sample calculation from this graph, if the overburden dip is  $10^\circ$ , then the smear is 0.083 and the sideslip is 0.054. So, if our overburden is 1 km thick, then this curve predicts a lateral-position error of 54 metres and a reflection-point smear of 83 metres.

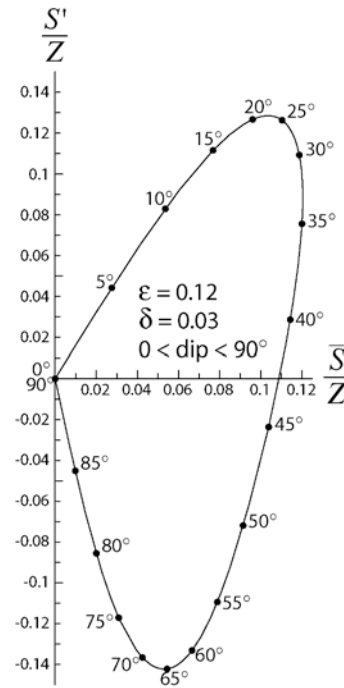


Figure 2.5 Parametric plot of normalized reflection-point smear versus average normalized sideslip with  $\epsilon$ , the dip of the anisotropic overburden, varying between  $0^\circ$  and  $90^\circ$ .

Note (Figure 2.5) that smear and sideslip are similar in maximum absolute magnitude. This offset dependence of the lateral-position error is as much a seismic-imaging pitfall as the lateral-position error itself. In subsequent chapters the reader will observe sharper, cleaner seismic images when we correct for velocity anisotropy, both sideslip and smear, in seismic migration.

### 2.1.3 The anisotropic velocity model

The application to 2D ADM using the TTI symmetry class is valid for the case where the symmetry axis is in the plane of the seismic section. The phase-velocity angle with respect to the symmetry axis  $\theta$  (Equation 1.2), sideslip velocity (Equation 1.5), and sideslip distance (e.g., Equation 2.2) all lie within the plane of seismic acquisition if that plane includes the axis of symmetry or bedding-plane normal. The assumption then for 2D ADM is that the acquisition of seismic data is in the direction perpendicular to the strike direction of the anisotropic overburden and the angle of bedding dip,  $\beta$ , is within the plane of the velocity model.

Figure 2.1 shows an interactive model-building display where the bedding dip is picked. The dips are drawn on a seismic display as 2D vectors. For the initial velocity model, dips and velocity boundaries are interpreted from the available seismic image for these data, usually a prestack time-migrated section processed assuming isotropy. The dips may be drawn to correlate with the dip of seismic events in the display or they may be drawn to correlate with other known dip information such as field measurements from surface or from well logs.

Important to note while discussing dips is that, in settings with complex geologic structures, the dip of anisotropic strata can be laterally varying, as shown in Figure 2.6. Whereas the values for  $\theta$  and  $\beta$  may not change in a given geologic unit, the dip of that unit may change dramatically. As we have seen here, specifically Figures 2.2 to 2.5, the direction and magnitude of sideslip and reflection-point smear change with overburden dip,  $\beta$ .

## 2.2 Algorithm implementation

My work on 2D ADM builds on a foundation of 2D Kirchhoff depth migration and an isotropic traveltimes generator, which were being used in production processing at a



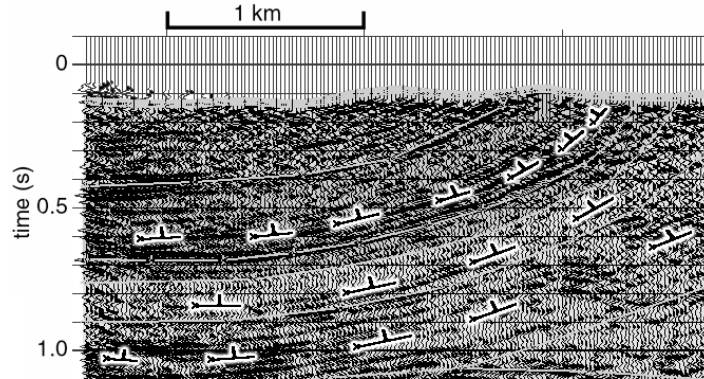


Figure 2.6 Interactive model-building display with dip picks applied to several layers.

commercial seismic-data-processing service provider. The traveltimes generator propagates wavefronts from each shot and receiver location down into the subsurface through a gridded velocity model with grid cells typically 50 m by 50 m in size. Seismic wavefronts separated by a constant time increment populate the 2D velocity field. A migration traveltimes field is then calculated by adding the shot and receiver traveltimes at each point in the model. In the isotropic case, each subsurface point along the wavefront curve moves forward in the direction normal to the wavefront for each time step in accordance with the model velocity local to that point.

The wavefield-propagation method is based on Huygens' principle, where each point on a wavefront is a source point for wave propagation. Huygens' Principle may be used to account for reflection and refraction, so refraction effects caused by velocity heterogeneity will be correctly managed by this algorithm. In the anisotropic case, variation in the dip of the anisotropic strata or other heterogeneities in the anisotropic parameters will also result in refraction of the wavefronts.

The only difference between the original isotropic Kirchhoff depth migration used for comparison purposes and the anisotropic algorithm developed for this thesis is in the traveltimes computation. Values for  $v_0$ ,  $\eta$ ,  $\epsilon$ , and bedding dip,  $\theta$ , are stored at each node of the anisotropic velocity-model grid. I modified the existing traveltimes calculator such that anisotropic group velocities, calculated using equations 1.3 and 1.4 in Chapter 1, are used to propagate the wavefront forward each step. In an anisotropic medium, the point on the wavefront moves forward along the group velocity vector, which is generally oblique to the

wavefront normal. Once source and receiver traveltimes are calculated, migration operators for a Kirchhoff depth migration are generated from the traveltimes.

Figure 2.7 shows an example of wavefronts propagating through dipping anisotropic strata. The wavefronts are separated by a constant time increment of 10 ms, with thicker lines at an increment of 100 ms. The wavefront plot may be considered a contour map of seismic traveltimes in the depth domain. This panel shows a traveltime map for one shot location on the physical-model dataset described by Isaac and Lawton (1999). When migrating a trace, the traveltime maps for the source and receiver are added together to create a traveltime map for that trace.

The Kirchhoff migration and the traveltime generator were written before this study by developers in the research department of Kelman Technologies Inc. Development for this thesis included definition of the anisotropic parameters in the velocity model and modification of the wavefront propagator such that anisotropic group-velocity vectors were calculated and used to propagate the waves forward at each time step.

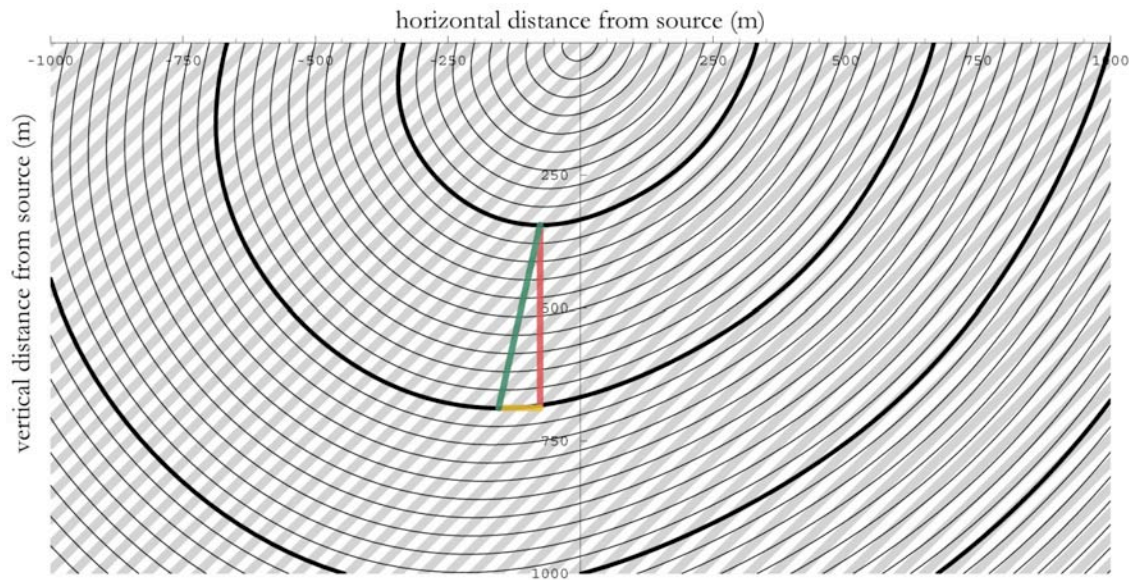


Figure 2.7 Source traveltime curves for physical-model dataset. Traveltime curves are separated by 10 ms and the bold curves are separated by 100 ms. The red segment represents a phase-velocity vector, yellow is the corresponding sideslip vector, and green is the group-velocity vector.



Figure 2.8 illustrates Huygens' Principle at work across a geologic boundary. In this case, the only thing changing across the vertical interface is the dip of the anisotropic strata. The seismic shot is in the media on the left of the figure, where the anisotropic strata are dipping  $45^\circ$  to the left. On the right half of the figure, across the vertical boundary the strata are dipping  $45^\circ$  to the right. If we consider each point on the wavefront to be a source for further wave propagation, then we can create a new wavefront at the next time step by superimposing group-velocity surfaces. The close-up view in the inset of this figure (Figure 2.8) shows how the calculation of the group-velocity vector at each point on the wavefront gives us a position on the new wavefront, if we divide the group-velocity magnitude by the time-step increment.

## 2.3 Algorithm testing

In testing the algorithm, I performed a prestack depth migration of the physical-model data from Isaac and Lawton (1999) discussed in section 1.3.3 of this thesis. Figure 2.9a shows a cross section of the model with the  $45^\circ$ -dipping anisotropic strata above a horizontal

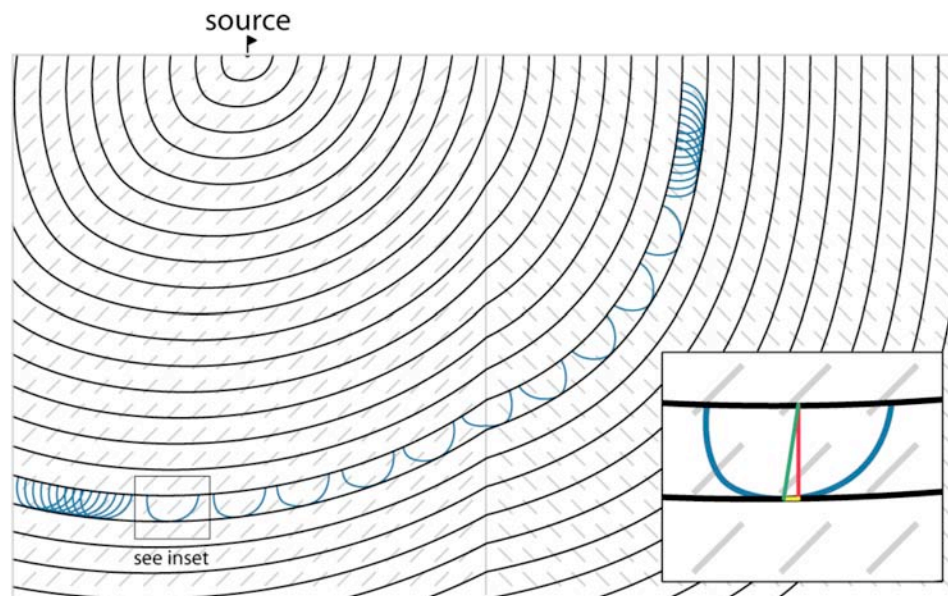


Figure 2.8 Source traveltimes curves illustrating Huygen's principle across a boundary with changing dip. Dip markers are shown in grey. Blue wavefront curves superimpose to make the next traveltimes curve. The inset shows the phase velocity (red), sideslip (yellow) vectors, and group velocity (green) vector, which, divided by the time increment, yields a point on the next wavefront.

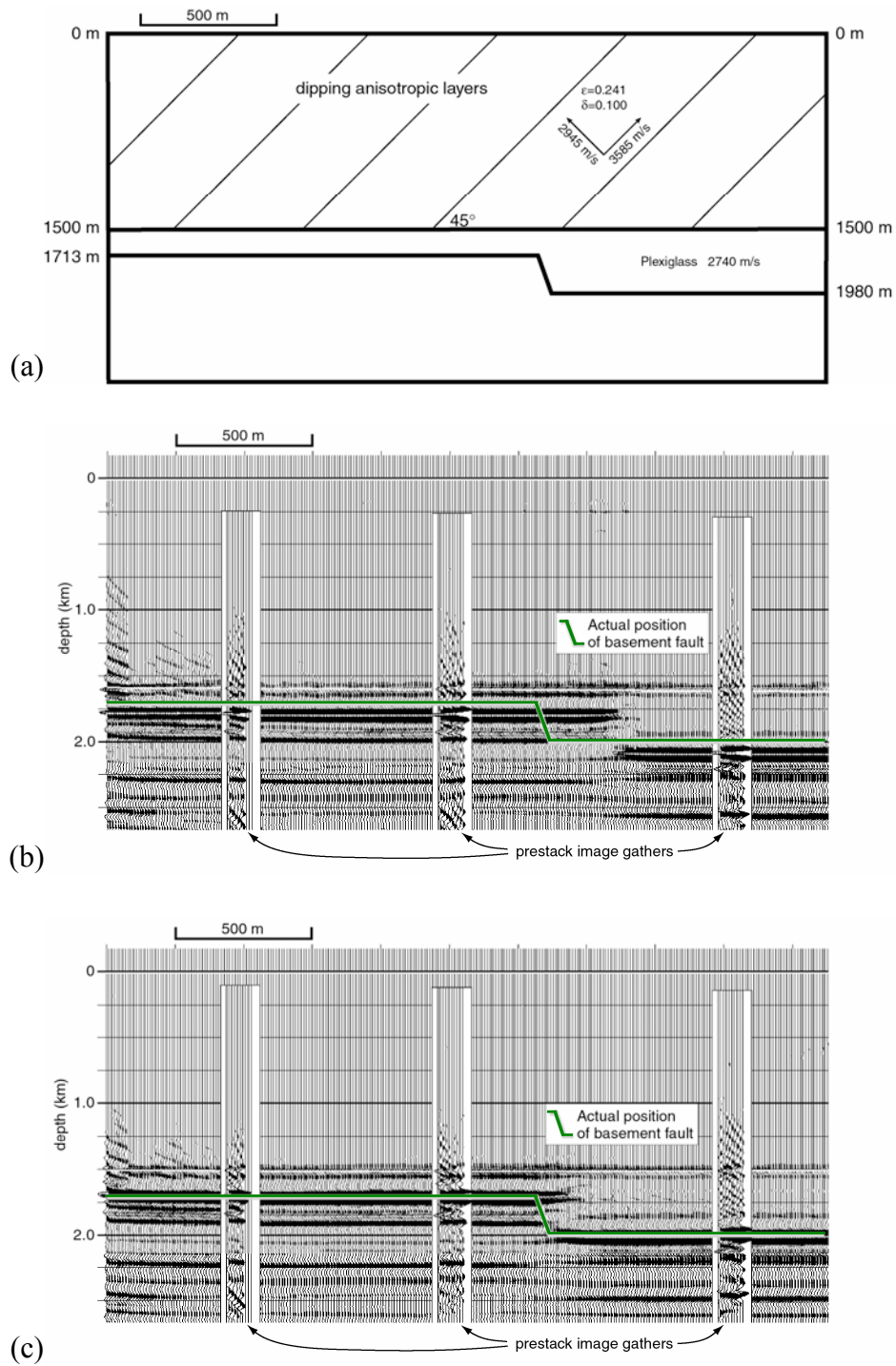


Figure 2.9 (a) Physical model from Isaac and Lawton (1999), (b) isotropic depth migration and (c) anisotropic depth migration of physical-model seismic data. Migrated image gathers are overlaid with offset increasing to the right.

imaging target. Isotropic depth migration was performed using velocities that provide optimum imaging, i.e., image gathers with minimum residual moveout as described in Section 1.2.4 on migration velocity analysis. The resulting seismic section is displayed in Figure 2.9b.

Note that the depths of the seismic reflectors on the seismic image (Figure 2.9b) are greater than the true depths of the imaged interfaces. Note also that the image gathers appear more or less flat with respect to offset. In order to flatten these image gathers, the model required a higher velocity than the true vertical velocity, so the image is deeper on the seismic display in Figure 2.9b than in reality. Depth-imaging practitioners commonly observe this phenomenon, where the seismic depths are greater than true geologic depths on a depth-migrated section (e.g., Schultz and Canales, 1997; Etris et al., 2001). The lateral-position error is, however, numerically larger in this example than the depth error. This 290-metre shift can be the difference between a successful hydrocarbon-exploration well and an exploration well that misses the target.

Figure 2.9c shows the migrated output after prestack anisotropic depth migration using the exact model parameters. The depths of the seismic events correlate well with the model depths and the major seismic events are flat on the image gathers. The seismic target is shifted laterally to a more accurate position. Most of the seismic events tie with the input model, although the top event shows a residual Kirchhoff migration artifact.

## 2.4 Summary

Anisotropic depth migration developed for this study corrects for lateral velocity heterogeneity and seismic velocity anisotropy. Anisotropic corrections were incorporated into a pre-existing depth-migration and model-building system designed to correct for lateral velocity heterogeneity.

The particular symmetry class of anisotropy handled by the algorithm is TTI with arbitrary and laterally varying dip. This ADM implementation is a 2D process, so this process also assumes that the symmetry axis is in the plane of seismic acquisition. This is the normal case when the seismic line is acquired perpendicular to the strike of the anisotropic overburden.



## Chapter 3

# Velocity model building

The accuracy of anisotropic velocity corrections is completely dependent upon the accuracy of the velocity model used in ADM. We need velocity-model diagnostics to assess the accuracy of the velocity model and we need a procedure for updating the velocity model with more accurate parameters after each iteration of migration.

This procedure does not attempt to derive physical properties of individual stratigraphic layers, but the goal is to find anisotropic parameters for large intervals in the velocity model that yields the most coherent seismic depth image. The approach to TTI velocity-model building developed is based on traditional prestack depth-migration analysis discussed in Chapter 1. Inspection of prestack image gathers and coherency on the stacked section from the resulting ADM directs modification of the anisotropic velocity model. Image-gather analysis for ADM is similar to the analysis used commonly in isotropic depth migration, except that additional anisotropic parameters in the velocity model are estimated.

This chapter looks at velocity model-building assumptions made during this study and the application of velocity-analysis methods to estimating parameters for TI media.

## 3.1 The velocity model

Before employing parameter-analysis methods, one must decide what information is required in a velocity model. Where a traditional seismic velocity model contains stratigraphic boundaries and the seismic velocity, anisotropic depth migration requires anisotropic parameters and, in the TTI case, the local orientation of the symmetry axis. In the method developed for this thesis, migration velocity, dip, and anisotropy parameters are stored in a gridded model, with grid cells typically 50 m by 50 m in size. The dimensions of this grid were selected to ensure that the resolution of the velocity grid is finer than the resolution of the migrated seismic data (Chen and Schuster, 1999) for a typical Canadian Foothills seismic survey with 3-km target depth and 40-Hz dominant frequency. As described in section 2.2.3 in the preceding chapter, the normal-to-bedding velocity,  $v_0$ , is stored at each grid node as

well as Thomsen's (1986) anisotropic parameters,  $\epsilon$  and  $\delta$ , which describe P-wave velocity behaviour for a TI medium. Since the dip of anisotropic strata in the overburden can vary significantly laterally and vertically in complex structural environments, each grid node also stores the tilt of the symmetry axis, which is assumed to be parallel to the bedding-plane normal.

It is also assumed that the symmetry axis is in the plane of the 2D seismic line. This 2D ADM then only applies to geologic settings in which the strike direction is consistent with depth and distance along the seismic line and where the acquisition direction is perpendicular to the strike of the anisotropic overburden. The depth-imaging practitioner interprets the dip from the seismic data in an interactive model-building display as shown in Figure 3.1. If this is the initial interpretation of the dip field, then the dips are picked from available seismic sections such as an isotropic depth-migrated section or a depth-converted time-migrated section.

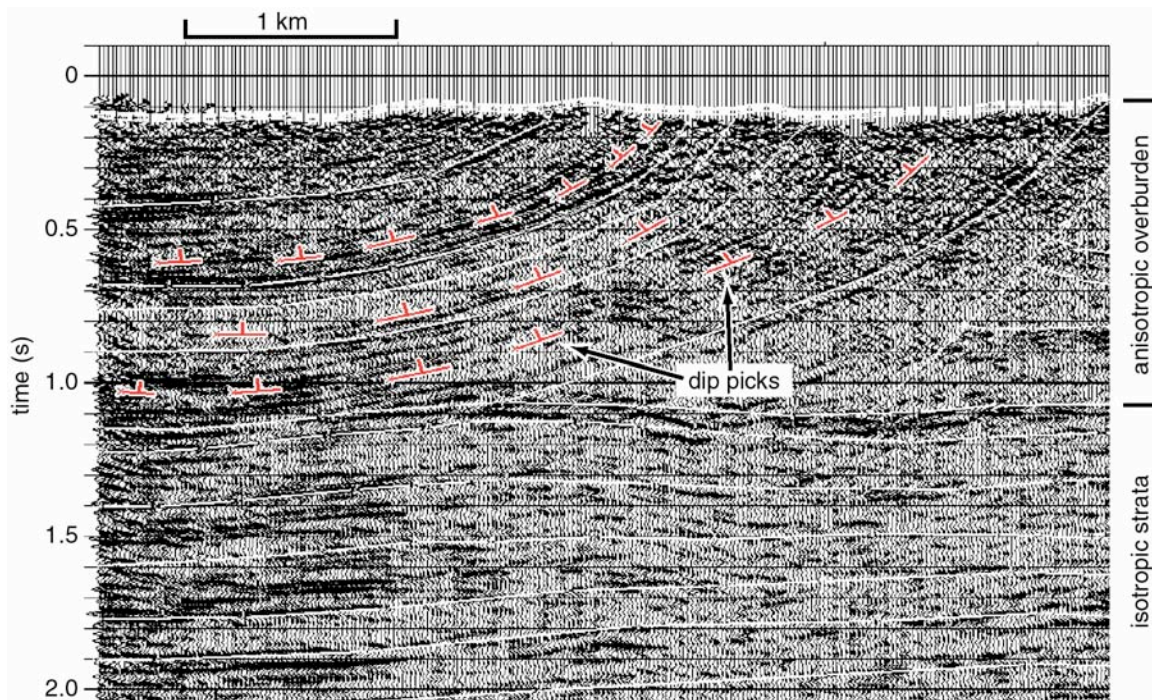


Figure 3.1 Interpreting dip from the seismic section. The white lines on the section are velocity-model zone boundaries. The dip may vary laterally within a zone as shown here. The upper section contains the shale-dominated clastic sequence, and the lower section contains carbonates that are assumed isotropic in the velocity model.



The strategy for picking velocity parameters developed in this thesis has the depth imager start with  $v_0$ , the parameter with the strongest influence on the migration, and then evaluate the parameters with a more subtle effect on the final migration,  $\eta$  and then  $\epsilon$ . If there are wells on or near the seismic line, the sonic log can be a good source for velocities for initial-model values for  $v_0$ . Because of the layering in the overburden, the well trajectory is often normal to bedding in the overburden clastics. As mentioned in Chapter 1, Schultz and Canales (1997) discuss the depth-imaging pitfall that seismic processing velocities are greater than well velocities when building isotropic velocity models. With anisotropic velocity-model building, the velocity model is parameterized with the normal-to-bedding velocity, which is usually the slowest direction.

With an initial model with interpreted dips,  $v_0$  from wells, and initial estimates of  $\eta$  and  $\epsilon$  based on regional refraction-survey data (Leslie and Lawton, 1999) or previous work in the area, velocity-model diagnostics enable fine-tuning of the anisotropic velocity parameters.

## 3.2 Image-gather analysis

Traditional image-gather velocity analysis, as described by Zhu et al. (1998), and discussed in Section 1.2.4 of this thesis, is employed as a velocity-model diagnostic. This prestack analysis method may be briefly described as follows: if a seismic event on a gather curves down or “frowns” toward the far offsets, then the model velocity is too high and, conversely, if the seismic event curves upward or “smiles”, then the model velocity is too low. If the seismic events have no residual moveout on the prestack gathers, the velocity above that event is correct.

As a strategy for anisotropic velocity-model building, the depth-imaging practitioner searches for a global velocity-model solution that produces the most consistent reflector continuity on prestack gathers. Figure 3.2 shows how anisotropy makes this task difficult and how the gathers can guide estimation of anisotropic parameters. Figure 3.2a is an interactive model-building display showing the west end of the Husky/Talisman data set from the southern Alberta Foothills described by Stork et al. (1995). The isotropic depth-migrated image is in the background with the velocity model and prestack image gathers also displayed. An approximate seismic aperture for the deeper event is shown adjacent to each gather.

Applying analysis of the “smiles and frowns”, the image gather on the right of Figure 3.2a

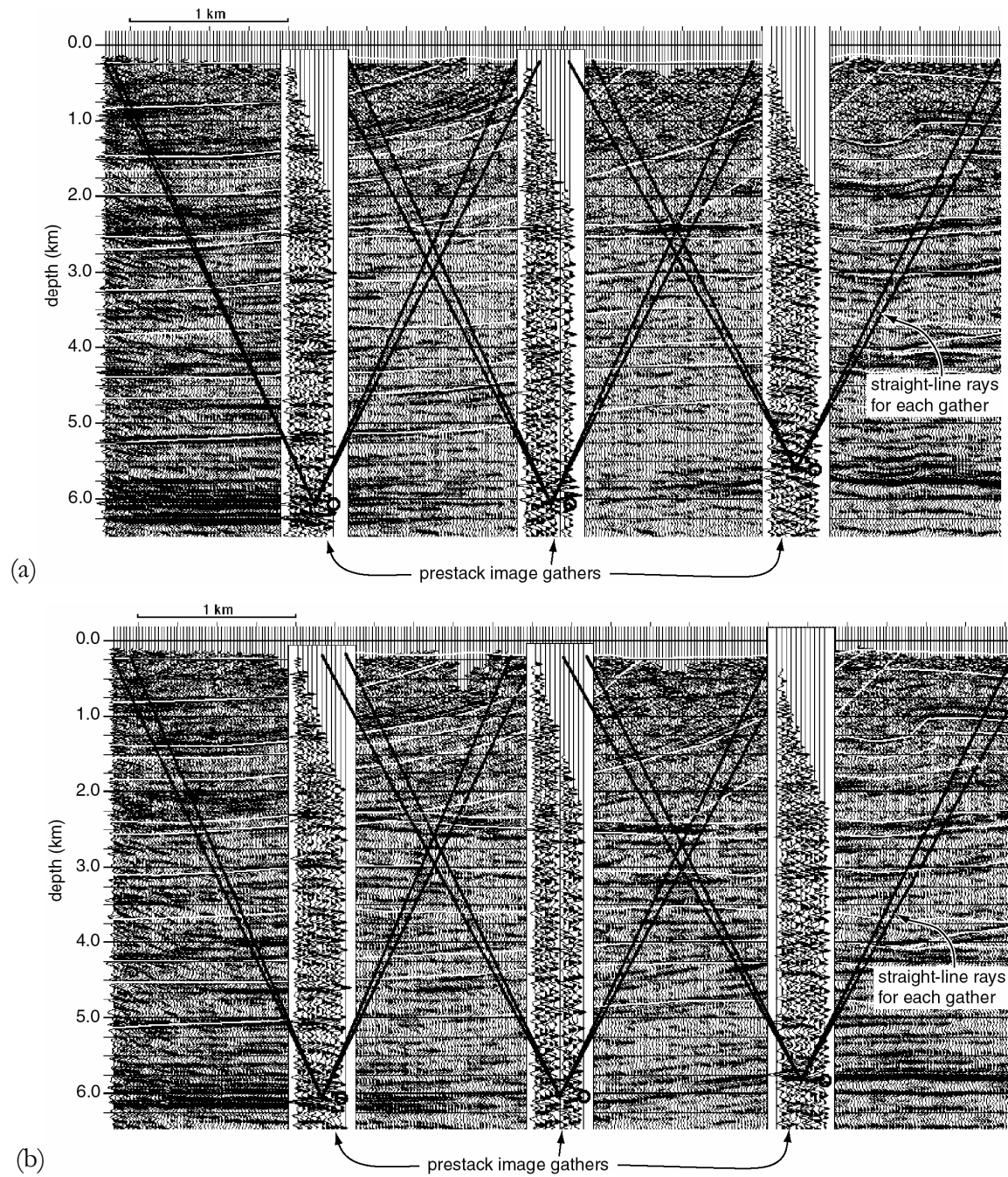


Figure 3.2 (a) Image-gather displays for the isotropic model, offset increasing to the right. The black lines represent a straight-line approximation of raytracing to the basement reflector at 6 km depth. (b) Image-gather displays for the anisotropic velocity model. Model parameters  $\epsilon = 10\%$  and  $\delta = 2.5\%$  are used for the clastic layers in the upper 2.5 km of the section.



needs a lower velocity to improve the final image and the gather in the centre needs a higher velocity for improvement. These two image gathers contain energy that has propagated through the same dipping shales as shown by the overlapping apertures in the overburden. A higher velocity in the model where the strata are steeply dipping will make the gather on the right “frown” even more and a lower velocity will make the gather in the centre “smile” greater. In this case, the model needs a higher model velocity parallel to bedding and a lower velocity normal to bedding if the migration is to produce image gathers with flat events.

Guided by these image gathers, I set the model value for  $\eta$  to 10% in overburden layers in the upper 2.5 km of the section. The normal-to-bedding velocity was decreased by 10%, and the seismic data were remigrated. The resulting section and gathers are shown in Figure 3.2b. The residual moveout on the gathers is reduced with these parameters in the anisotropic migration. The noisy gather in the centre is flatter and the stack in the background shows improved lateral continuity of reflectors. The gather on the right shows the most dramatic improvement in residual moveout and again the reflector on the stack has improved in continuity. I applied these velocity-model updates to this seismic dataset and the final migrated results are presented and discussed in Chapter 4.

Adjusting the anisotropic velocity parameters reconciled the conflicting residual moveout given by neighbouring image gathers after isotropic migration. The apparent conflict in velocities guided the development of optimum velocity-model parameters.

### 3.3 Stack-image analysis

Some datasets in thrust-belt environments do not have enough prestack coherency for prestack velocity analysis. There is also a danger with prestack analysis of focussing on individual gathers at the expense of the overall image quality. In addition, residual-moveout analysis on image gathers ignores any reflection-point smear effects described in Section 1.1.2 that will be minimized by optimum velocities. As a safeguard against these potential pitfalls of prestack velocity analysis, stacks of prestack migrated seismic data with varying velocity parameters are compared for coherency and amplitude of seismic events.

Figure 3.3 shows three seismic sections, prestack depth-migrated with scaled percentages of the original velocity function. Note that although there is only 2% change between adjacent background velocity functions, there are noticeable changes in reflector continuity in the

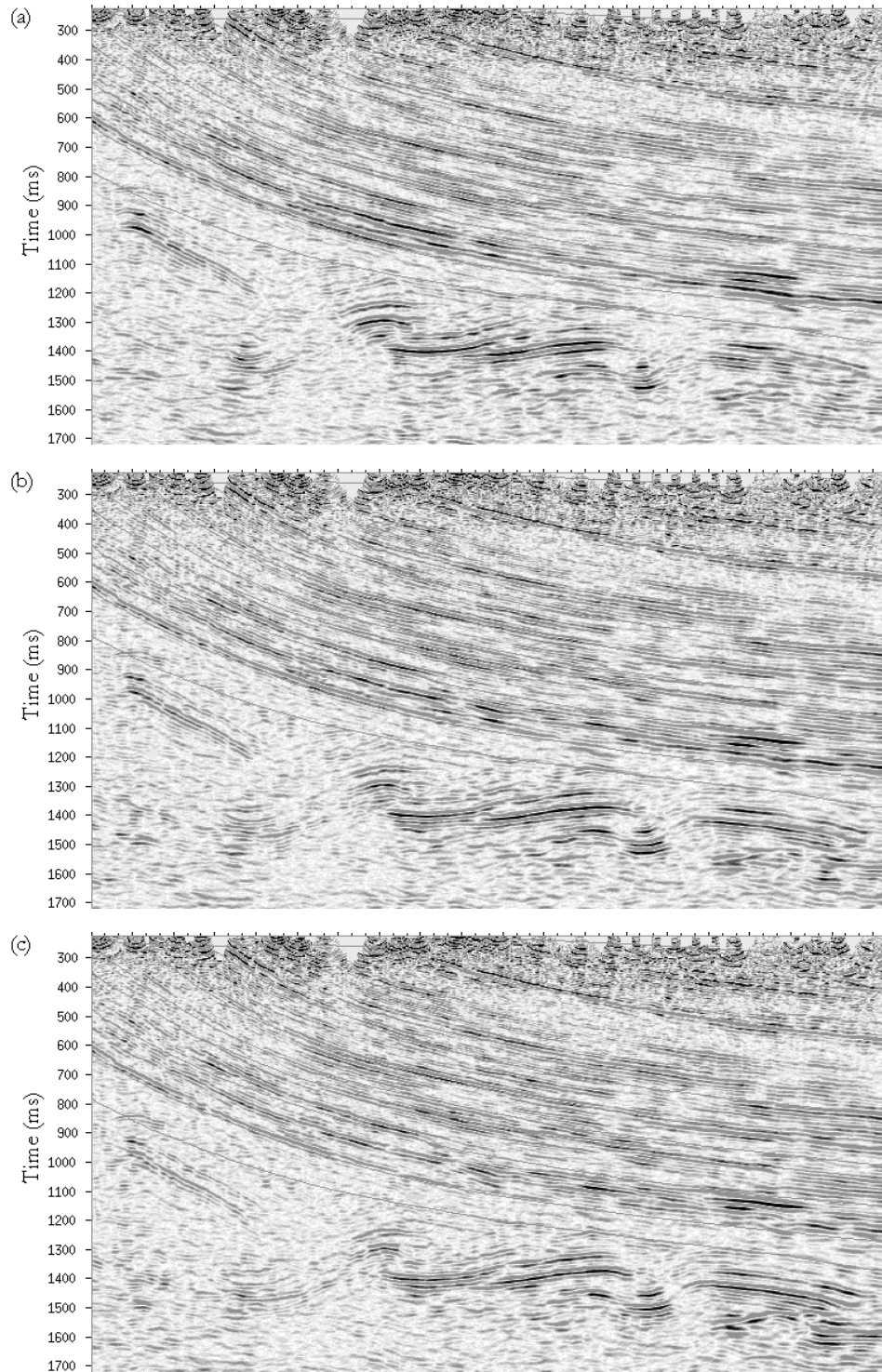


Figure 3.3 Prestack depth-migrated sections with varying migration velocity. (a) migrated with the base velocity function scaled to 98%, (b) migrated with 100% of the base velocity function and (c) migrated with the velocity scaled to 102% of the base velocity function.

deeper target structures.

After iterating over  $v_0$ , migrations were tested for different values of  $\epsilon$  with  $\delta$  held constant at  $\delta = 0$ . Figure 3.4 shows three seismic sections with  $\epsilon$  ranging from 0 to 16% in steps of 8%. Two things to note here are the changes in image quality and the change in lateral position of target structures among the three sections. After inspecting migrated images with values for  $\epsilon$  in 2% intervals, the value of  $\epsilon = 8\%$  was chosen as the best image, with the most consistent reflector character for the structured target events below 1000 ms. Once a value for  $\epsilon$  was selected, values of  $\delta$  were varied and images examined.

Figure 3.5 shows the prestack migrated sections with  $\epsilon$  fixed at 8% and values for  $\delta$  of 0, 8%, and 16%. That there is negligible change in the lateral position of the target structures, but there is an improvement in reflector continuity and more consistent reflector character when  $\delta = 8\%$ . The resulting anisotropic depth migration using these parameters is compared to time migration and to traditional depth migration in Chapter 4.

### 3.4 Directional image gathers

The dip-oriented-offset method is proposed in this thesis as an interpretive tool to diagnose problems with the anisotropic velocity model and to guide velocity-model updates. In traditional prestack image gathers, traces migrated to an output CDP are binned using the common-offset method. Traces falling within a certain range of source-receiver offsets are stacked together in an offset bin and several offset bins make up a common-offset image gather. For example, an image gather may contain 30 traces ranging in offset from 0 to 3000 in 100-meter wide offset bins: 0-100, 100-200, ..., 2800-2900, 2900-3000, regardless of the sign of the offset.

Dip-oriented-offset image gathers are binned differently. As a trace is depth migrated to an output CDP location, it falls in an offset bin defined by:

$$h_d = \sqrt{h^2 + x^2} \quad 3.1$$

where  $h_d$  is the dip-oriented offset, defined as the vector sum of  $h$ , the source-receiver offset, and  $x$ , the migration offset. The only difference between the traditional method and the dip-



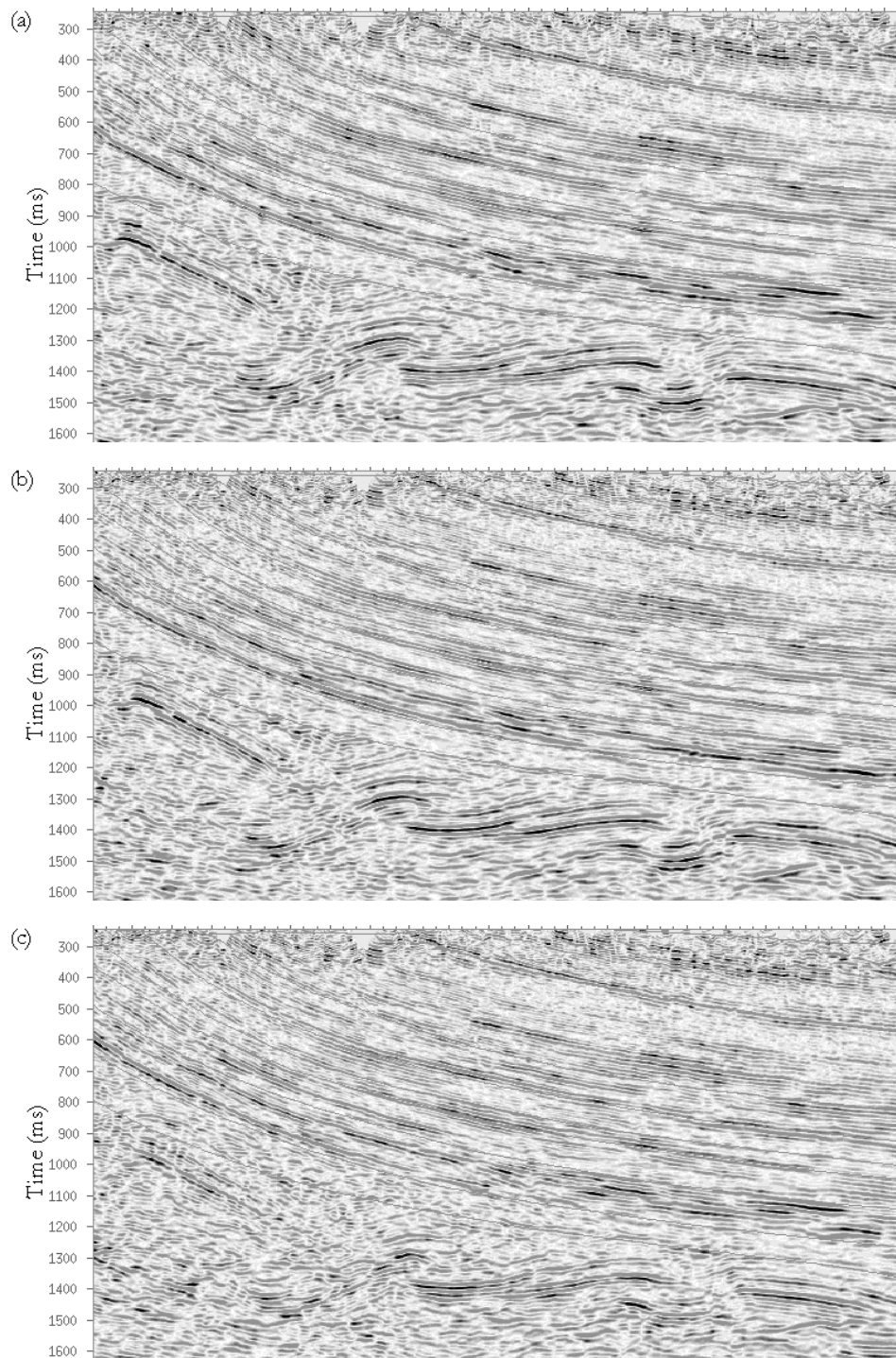


Figure 3.4 Prestack depth-migrated sections migrated with varying values for  $\Delta$  ( $\Delta = 0$ ). (a) migrated with the isotropic case where  $\Delta = 0$ , (b) migrated with  $\Delta = 8\%$  and (c) migrated with  $\Delta = 16\%$ . Note changes in reflector continuity and in lateral position of the target reflector on the left of the section at 950 ms.

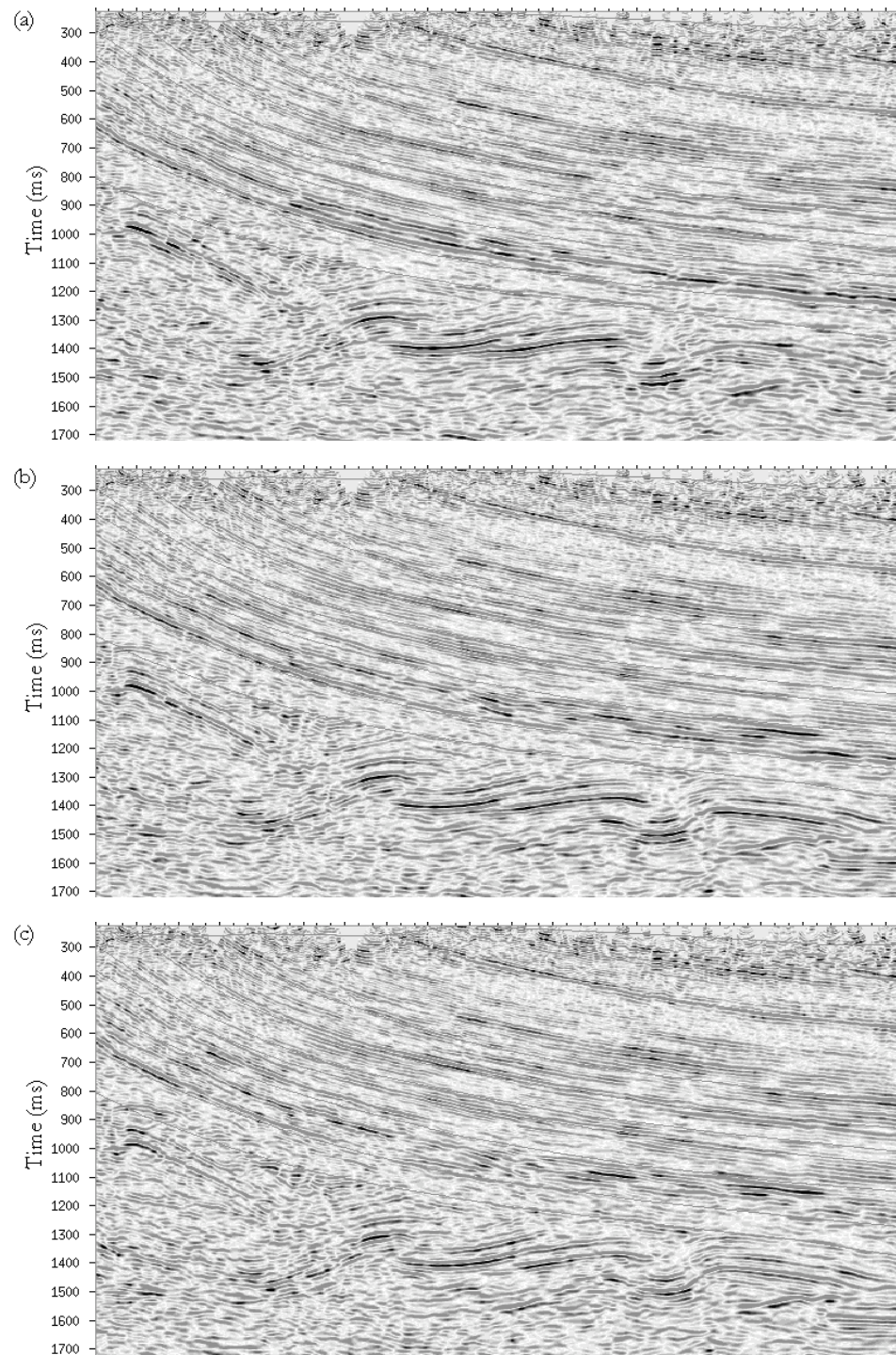


Figure 3.5 Prestack depth-migrated sections migrated with varying  $\epsilon$  and  $\epsilon = 8\%$ . (a) migrated with the isotropic case where  $\epsilon = 0$ , (b) migrated with  $\epsilon = 8\%$  and (c) migrated with  $\epsilon = 16\%$ . Note the change in reflector continuity with negligible change in lateral position of the target events.



oriented-offset method is in the binning of the prestack gathers. The same anisotropic raytracing and Kirchhoff depth migration is employed, but migrated traces are assigned to dip-oriented-offset bins instead of common-offset bins.

### 3.4.1 Physical-model data example

Again we revisit the physical model seismic data from Isaac and Lawton (1999) discussed in sections 1.3.3 and 2.2 of this thesis. Depth-migrated gathers from these data illustrate the differences between common-offset image gathers and dip-oriented-offset image gathers (Figure 3.6). The relatively noise-free prestack domain of physical-model data emphasizes the contrast between the two binning methods.

Figure 3.6 shows prestack image gathers from the anisotropic step model: one using the

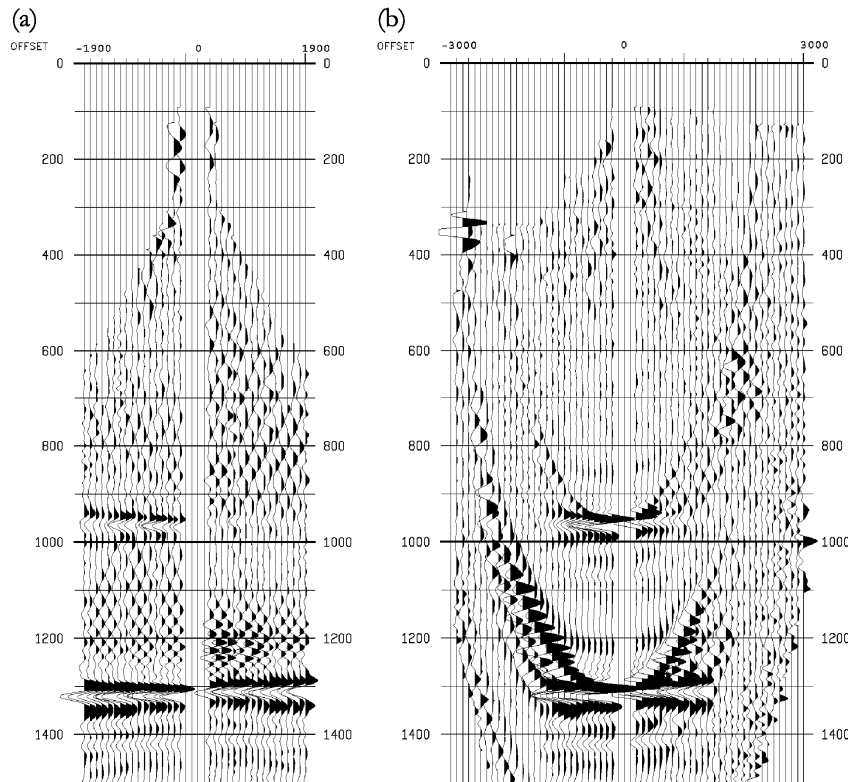


Figure 3.6 (a) common-offset image gather and (b) dip-oriented-offset image gather from the anisotropic step model. Note that the migration operator noise creates a checkerboard pattern obscuring upper reflectors on the common-offset image gather in (a) and the migration operator noise is coherent out to the far offsets on the gather in (b).

common-offset binning method and one using the dip-oriented-offset binning method. The common-offset image gather (figure 3.6a) shows a bright, flat event at 1325 ms and another flat event at 975 ms which is somewhat obscured by migration operator noise. The dip-oriented-offset image gather (figure 3.6b) shows the same events, but noise from the migration operator is on the far dip-oriented offsets and therefore does not interfere with the clear reflection signal at 975 ms.

Another interesting observation from these data is in the lateral position of the flat events. The events are not centred at the zero offset, but are slightly shifted to the left, as is readily apparent in the event above 1000 ms. This is the lateral shift required of the migration to correctly position the structure below the dipping anisotropic strata. Because the dip-oriented offset has a migration-distance term, the migration move appears on the prestack gather in the lateral placement of energy.

### 3.4.2 Field data example

A field-data example from the Rocky Mountain thrust-and-fold belt was chosen to further illustrate the directionality of the dip-oriented-offset image gather and to show a practical application of the method (Figure 3.7).

An anisotropic depth migration for the Amoco data set, discussed in Section 3.3, is displayed in Figure 3.7a. Figure 3.7b shows a dip-oriented-offset gather and Figure 3.7c shows a common-offset gather, both at the location marked on the section in Figure 3.7a. At just above 1 second at this trace location on the stack (Figure 3.7a), there is a bright reflection that dips gently to the right of the section. At the same time on the image gather (Figure 3.7b), there is coherent energy on the right side of the image gather. Further down the section, events dip to the left of the section at 1100 ms in Figure 3.7a and the corresponding events appear on the left side of the dip-oriented-offset image gather in Figure 3.7b.

The directionality of the image gather helps interpret the prestack data so that the seismic-data processor or interpreter can focus in on the geologically significant seismic events. In the above example, the velocities above 1000 ms should be evaluated because the event dipping to the right shows some residual moveout on this gather.

Directionality of the gather allows certain dips to be removed from the section by simply muting the gathers. If there are east-dipping signal and west-dipping noise, one can use a

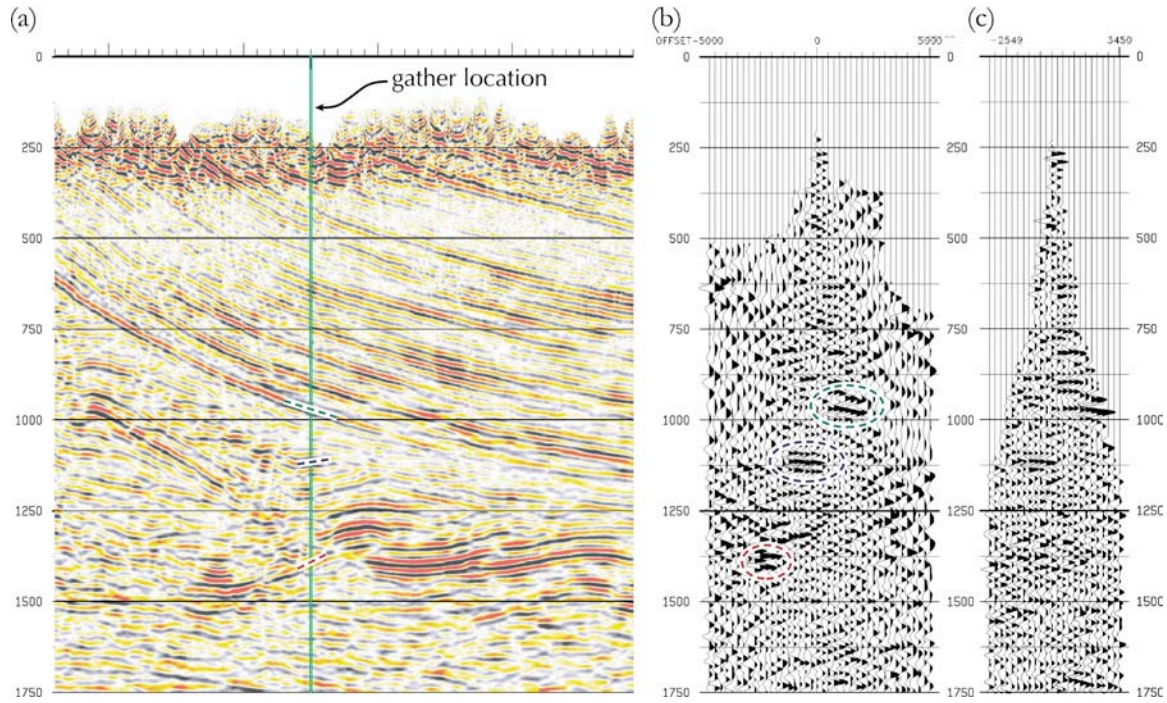


Figure 3.7 (a) region of depth-migrated stack showing location of (b) the dip-oriented-offset image gather. Seismic events inside dashed ellipses on the gather in (b) correspond with the dipping seismic events on the stack marked with dashed lines in (a). (c) shows the same gather in the common-offset domain.

harsher mute on the west side of the gather. In this field example, I observed some steeply dipping migration noise on the section. Figure 3.8a shows this part of the section. After muting the dip-oriented-offset image gathers, the section in Figure 3.8b has less noise apparent. Note the coherent migration noise outlined in the boxes in Figure 3.8a and the reflector continuity revealed in Figure 3.8b when the migration noise is muted from the gathers. Also there is an improvement in amplitude of near-surface reflectors in Figure 3.8b. Because of the migration-offset term in the dip-oriented-offset equation, a mute in the dip-oriented-offset domain may be employed as a laterally varying dip filter that can be picked interactively after migration.

### 3.5 Summary

If carefully applied, traditional methods of velocity model analysis and quality control can be very effective in estimating anisotropic parameters for seismic imaging. Described in this chapter are applications of prestack and poststack methods for estimating anisotropic



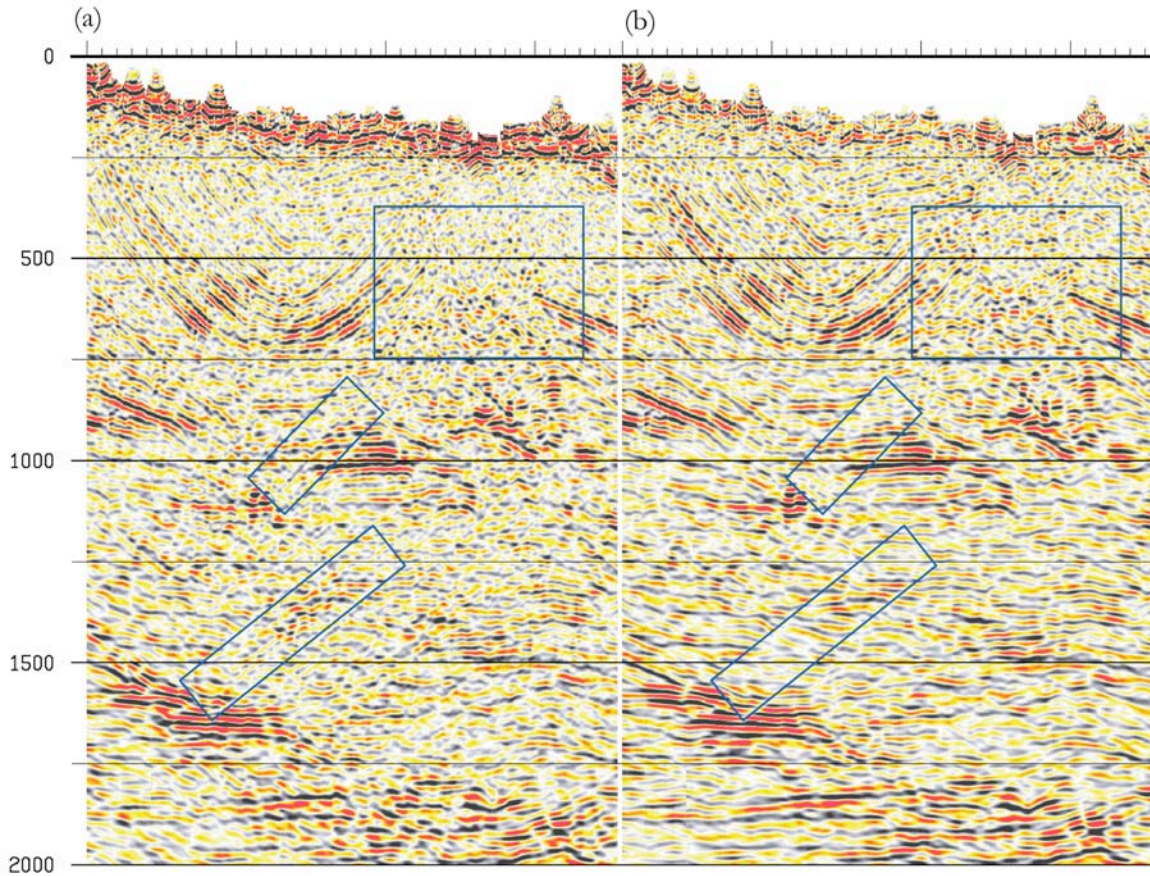


Figure 3.8 Prestack migrated section using the dip-oriented-offset method (a) with no mute applied to the gathers before stack and (b) with mute applied to the gathers before stack. The boxes highlight linear noise trains that are removed after mute is applied.

velocity parameters.

The goal of model building for ADM is simply to find a comprehensive velocity model that offer the most accurate seismic image and positioning of subsurface targets. Whereas seismic imaging parameters are not resolvable to the degree that the anisotropic parameters from ADM are useful for detailed lithology prediction, other independent measurements such as well logs, cores, refraction surveys, and VSP analysis may provide additional constraints on some parameters of the velocity model.



## Chapter 4

# Case Histories

The objective of this research is to develop a methodology that will improve imaging and positioning of structures on seismic images below dipping anisotropic strata. The ultimate test to determine the effectiveness of this methodology is to apply the process to field data used in resource exploration. The area of interest for these case histories is the Canadian Rocky Mountain thrust and fold belt. Anisotropic depth migration is well suited to this geographic region because of the diversity of dipping geometries in the overburden and the exploration targets below.

Each of these seismic-data-processing case histories includes the application of depth-migration velocity analysis as described in Chapter 3. A depth-migration project typically includes velocity model building and depth migration. Before these processes can be applied, preprocessing of seismic data through a typical time-processing runstream, as described by Yilmaz (1987), for example, must be applied to the data. The processes applied to these data followed a typical processing sequence for complex-structure land data, as outlined in Table 4.1.

Three contrasting seismic-data-processing case histories were chosen to show the effectiveness of this method. The first example is a public-domain dataset that is considered a standard dataset for seismic imaging in a thrust-belt environment. Significant imaging problems on these data were resolved with anisotropic depth migration. The second shows a subtler imaging problem with corresponding subtle imaging enhancements when we correct for seismic anisotropy. The final example is a natural-gas exploration case history that shows how anisotropic depth migration was used to correctly position a subsurface reflector after initial drilling missed the target.

## 4.1 Benjamin Creek

The Husky/Talisman dataset is a public-domain seismic dataset from the southern Alberta Foothills described by Stork et al. (1995). This 2D line is intended for use as a showcase

Process	Description
Refraction statics	Static correction for near-surface velocity variations derived from first-arrival seismic energy.
f-k filter	Suppress noise
Spiking deconvolution	Boosts higher frequencies and sharpens seismic wavelet
Surface-consistent reflection statics	Calculate statics by cross-correlating seismic traces and solving for static shifts consistent with time delays between shots or receivers.
Prestack migration	Prestack time migration is a standard process in complex-structure land areas. Prestack anisotropic depth migration replaces prestack time migration.

Table 4.1 Processing steps used in data preparation for prestack depth migration.

dataset for testing and demonstrating the effectiveness of seismic imaging algorithms. Here I compare the effectiveness of isotropic versus anisotropic depth migration on these data.

The original (isotropic) velocity model was parameterized for an anisotropic depth migration with the required dip information as described in Chapter 3. Only the shale-dominated clastic layers in the upper part of the section were considered anisotropic in our model. Parameters determined from refraction-survey measurements on shales with near-vertical bedding dip by Leslie and Lawton (1998) on dipping shales in the Alberta Foothills helped to constrain the anisotropic velocity model. In two separate field locations,  $\epsilon$  was found to be near zero for an  $\delta$  of 0.14 and 0.26. Since  $\epsilon$  is small and changes in  $\epsilon$  have a subtle influence on  $s$  (equation 2.1), I parameterized the model with  $\epsilon$ . I set  $\epsilon$  to be one-quarter of  $\delta$  and iterated to find the value of  $\epsilon$  that produced the flattest prestack image gathers. If possible, a complete anisotropic velocity model should contain estimates for both  $\delta$  and  $\epsilon$ .

Initial values of anisotropic parameters were  $\delta = 15\%$  and  $\epsilon = 3.8\%$ , based on field measurements by Leslie and Lawton (1998) for similar rocks, and the initial  $v_0$  was based on an isotropic depth-migration velocity analysis beneath the horizontal anisotropic layers. After a few revisions to the model, guided by the inspection of image gathers, optimum imaging was achieved for  $\delta = 10\%$  and  $\epsilon = 2.5\%$ . Once the image-gather conflict shown in Figure 3.4 of Chapter 3 was resolved, I inspected the image gathers again for improvements in flatness of gathers with a change in  $v_0$ .

A comparison between the final anisotropic depth migration and the final isotropic depth migration is shown in Figure 4.1. Differences observed between the sections are attributed only to differences between the isotropic and anisotropic migrations. The highlighted rectangles on both sections in Figure 4.1 show some of the key improvements of anisotropic depth migration when compared to isotropic depth migration. Boxes A and A' show differences beneath the dipping strata: there is a lateral movement and improvement in reflector continuity below the fault contact in the upper left corner of A' compared with that of A. The reflector that spans the bottom of A' also shows improved continuity. The anticline interpreted in box B (Figure 4.1a) is not present in B' (Figure 4.1b). The anticline in B is considered to be a false depth structure caused by a significant change in near-surface dips. Basement reflector continuity is also improved after anisotropic depth migration, as evident by comparing boxes C and C'.

ADM resolved the image-gather conflict documented in Section 3.2 and improved the seismic imaging below the steeply dipping clastics. A more complete representation of the overburden velocities yielded significant improvements on the seismic image.

## 4.2 The Triangle Zone

A second data example is from the triangle zone in the Alberta Foothills. This dataset shows less dramatic variation in overburden dips than the Benjamin Creek dataset and the imaging problems are more subtle. The following sections show a detailed comparison between prestack time migration, prestack depth migration, and prestack anisotropic depth migration.

If the reader wishes to refer back to the methodologies of Chapter 3 as applied to these data, he/she should note that the velocity model was built using the stack-image analysis method of Section 3.3. Stack images for this dataset with varying anisotropic velocity parameters are shown in figures 3.3, 3.4 and 3.5.

### 4.2.1 Velocity models

Each of the three migrations presented here requires a model of the seismic velocities. The different assumptions inherent in the migrations will require differences among velocity models to accommodate the assumptions made. In the case of time migration, the migration is based on a velocity equation depending on RMS velocity, so we don't expect the velocities



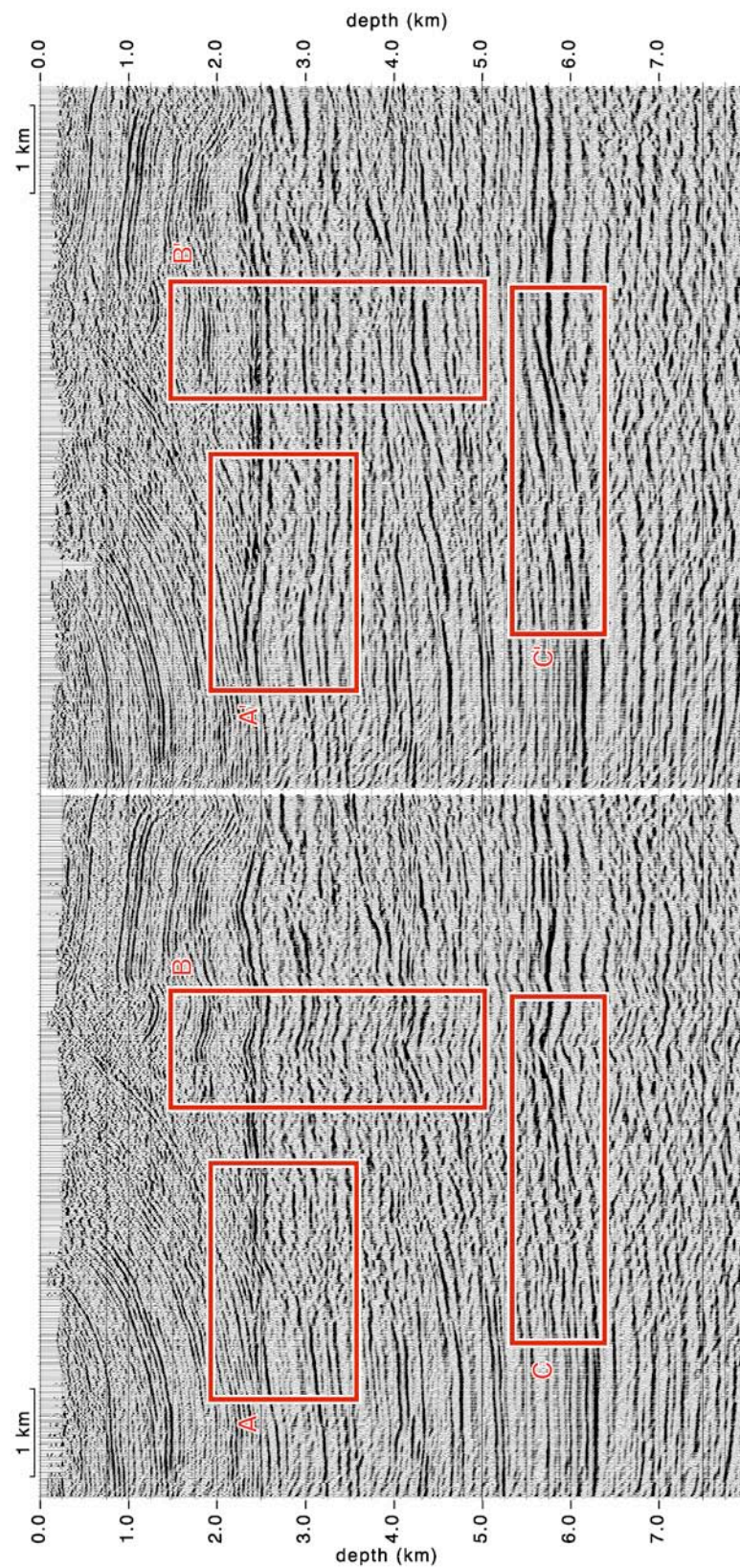


Figure 4.1 Depth migrated sections with (a) isotropic and (b) anisotropic migrations. Boxes outline some key differences in imaging.

necessarily represent the geology. For isotropic depth migration, the velocity model looks more like a geologic cross section, but the isotropic assumption means that we ignore the velocity increase as the direction of seismic wave propagation goes from bedding-normal to bedding-parallel, so our model requires velocities greater than the normal-to-bedding velocities for optimum imaging. In the case of 2D anisotropic depth migration, our optimum-imaging velocity model will more accurately reflect the geologic velocities insofar as there are no significant out-of-plane imaging or anisotropy effects.

We see the aforementioned velocity characteristics in the velocity model display for each respective migration of this dataset. Figure 4.2a shows the interval-velocity map used in the time migration and Figure 4.2b shows the velocity map used in the depth migration. Note that the depth migration shows more detailed geologic information, with structurally deformed stratigraphic layers in the overburden. The anisotropic velocity model, shown as a map of  $v_0$  in Figure 4.2c, has the same detail as the isotropic velocity model (Figure 4.2b), but the overall magnitude of the velocities in the anisotropic model is noticeably lower than that of the isotropic velocity model. The isotropic depth migration ignores anisotropy, so velocities higher than the vertical velocities were used to obtain an optimum image.

The next section shows the seismic sections resulting from each migration method and its associated velocity model.

### 4.2.2 Migrated sections

The migrated seismic sections that employed these three velocity models are displayed in Figure 4.3. For ease of comparison, each of the two depth-migrated sections was vertically scaled back to time using its respective velocity model. The vertical black line near the left edge of each section is displayed at a constant position to illustrate the lateral position change of the imaged structure beneath. From the time-migrated section (Figure 4.3a) to the depth-migrated section (Figure 4.3b) there is a lateral-position change of 175 m on the crest of the seismic reflector below the black line. This lateral-position change corrects for raybending in the near-surface resulting from lateral velocity variation shown in the depth-migration velocity model (Figure 4.2b). The next lateral position change, between depth-migrated and anisotropic-depth-migrated sections (Figures 4.3b and 4.3c), corrects for sideslip resulting from dipping anisotropic strata above the target. This lateral shift of 90 m, in addition to the 175 m from raybending, gives a total lateral-position error for this target

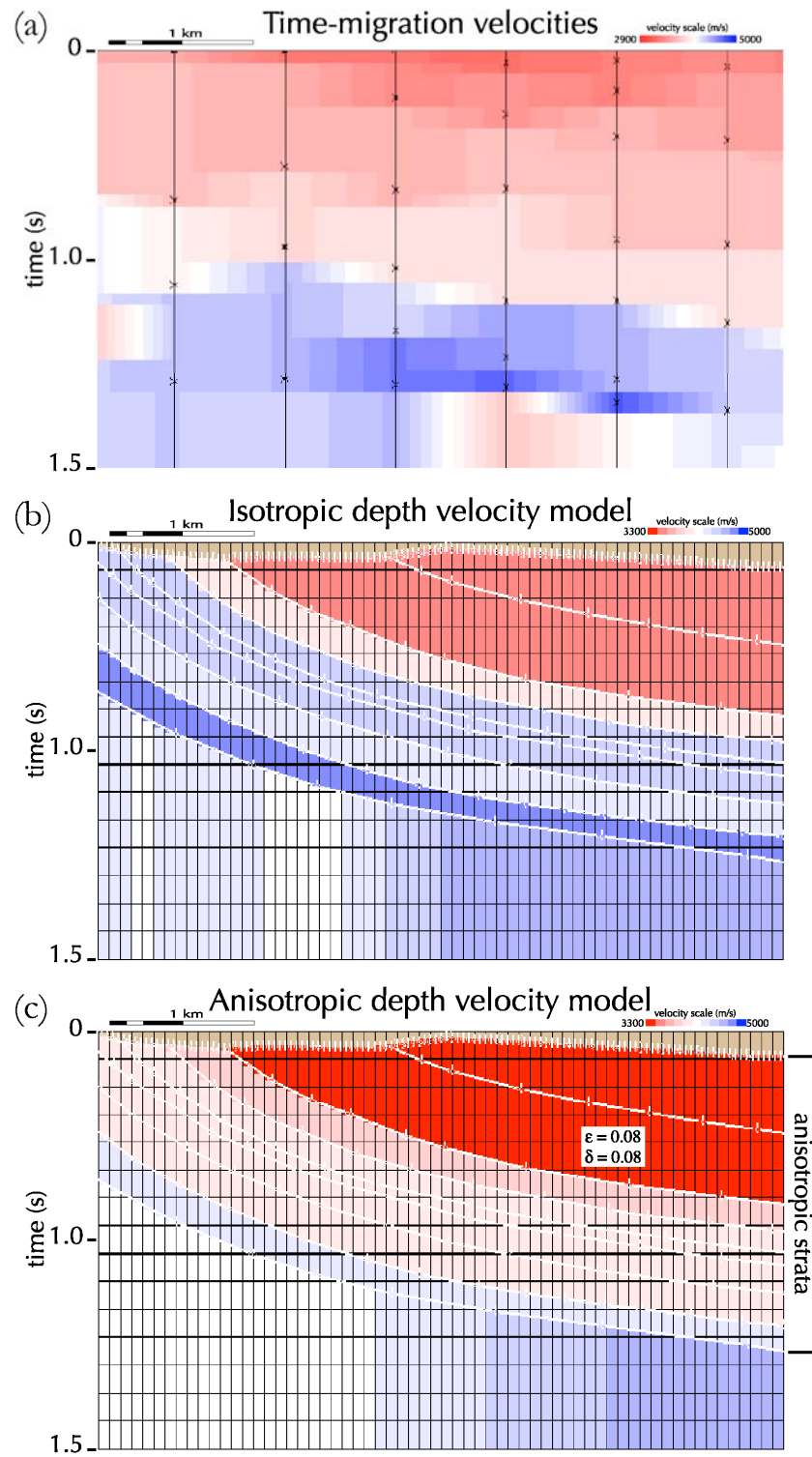


Figure 4.2 Velocity maps for (a) time migration, (b) isotropic depth migration, and (c) anisotropic depth migration as applied to the Triangle Zone dataset.



event on the time-migrated section of 265 m. As we more accurately represent the velocity field, we more accurately position the seismic reflectors.

A more accurate velocity field should also yield imaging improvements on the final section, as we observed in Section 4.1. Because this area does not pose as dramatic an imaging problem as in Benjamin Creek (Section 4.1), the changes in seismic imaging are not as dramatic. However, the target events across the bottom of each section in Figure 4.3 have sharper reflector terminations and image steeper dips as we compare time migration (Figure 4.3a) to depth migration (Figure 4.3b) and again when we compare depth migration to anisotropic depth migration (Figure 4.3c).

Another indication of accurate velocities is the accuracy of depth position of target reflectors. Figure 4.4 shows depth migrations for isotropic (Figure 4.4a) and anisotropic (Figure 4.4b) algorithms. The red marker indicates the depth to the target horizon outlined in green as measured from well logs. Note that the traditional depth migration shows the target as being 175 m deeper than the well measurement indicates. This is consistent with observations of Schultz and Canales (1997) and Etris et al. (2001) that the seismic depth is typically greater than well depth with traditional depth migration. These authors describe a commonly used imaging method where one isotropic velocity model is used to optimize the seismic imaging, and another velocity model with lower velocities is used to scale the depth migration to deliver accurate reflector depths. Whereas optimum-imaging velocities may be estimated from seismic-velocity analysis, the velocity model that yields accurate reflector depths cannot.

In contrast, when we directly account for seismic velocity anisotropy in our migration (Figure 4.4b), model velocities higher than geologic velocities are not needed for optimum imaging. Figure 4.4b shows a depth error of approximately 20 m, which is within a seismic wavelength and less than 1% of the depth to the target. In one migration with one velocity model, this method has the potential to deliver an optimum image and accurate reflector depths.

### 4.3 The Nordegg sidetrack

This exploration objective was a natural-gas development target in the Central Alberta Foothills. The Mississippian target was interpreted as having been carried on a major thrust

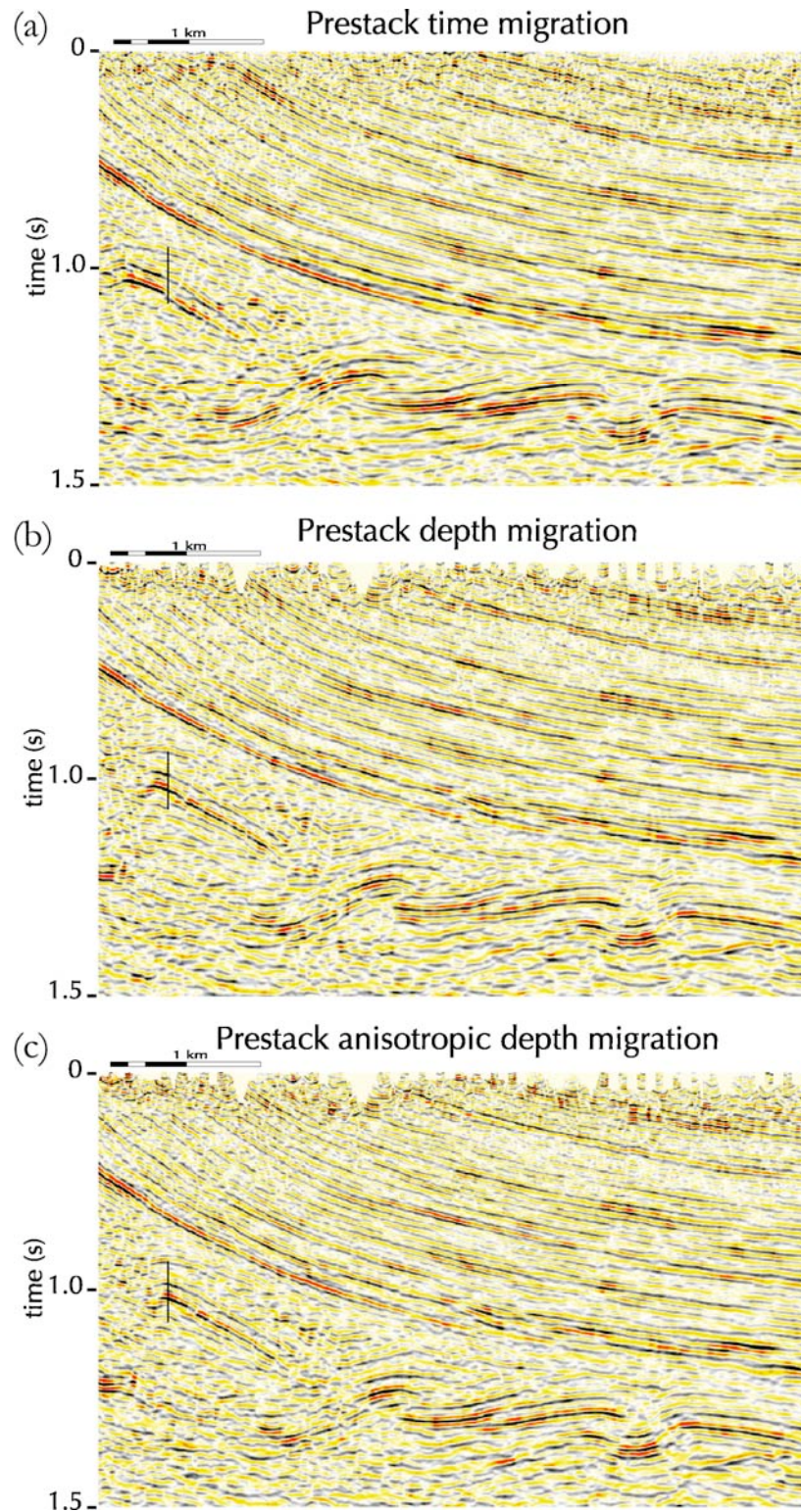


Figure 4.3 (a) Prestack time migration, (b) isotropic depth migration, and (c) anisotropic depth migration displayed in time for the Triangle Zone dataset.

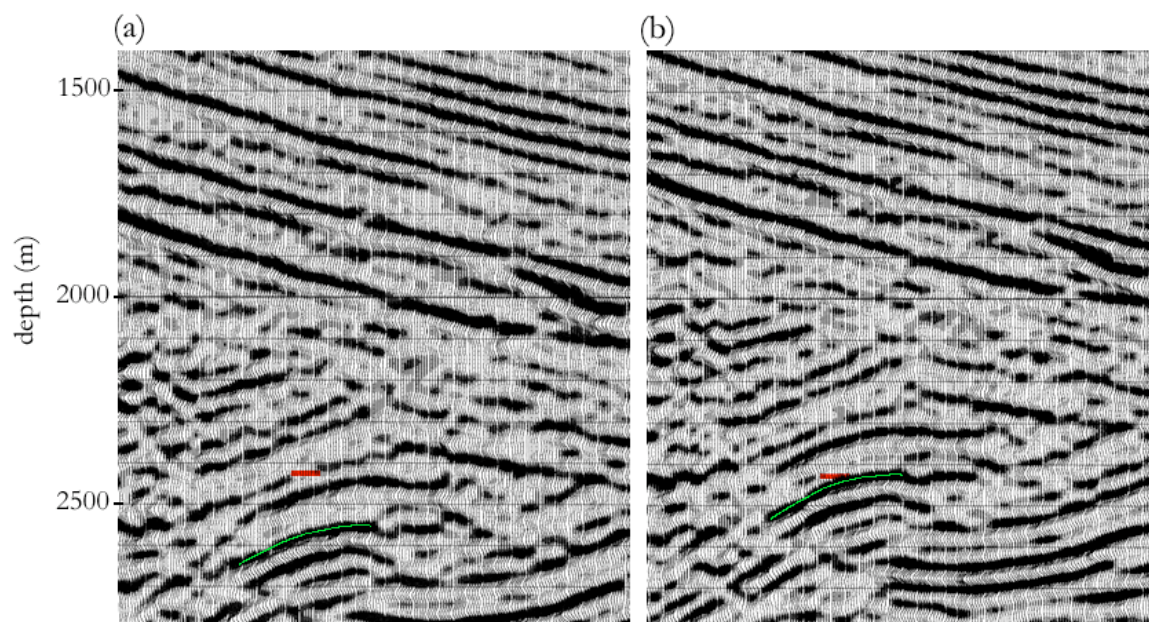


Figure 4.4 Correlation between well depth and seismic depth for (a) isotropic depth migration and (b) anisotropic depth migration. The red marker is the well depth that correlates to the seismic event traced in green.

sheet with a lateral extent of approximately 30 km trending in a NW-SE strike direction. Several producing wells exist on the field.

A well was proposed by explorationists at Suncor Energy Inc on the basis of a seismic line acquired by Response Seismic Surveys Ltd in 1992. The structural targets proposed for the well range in depth from 3000 to 3350 m and are located beneath the Southwest flank of a major triangle zone. Figure 4.5 shows the poststack-time-migrated section of the Response data set showing a dry and abandoned well from 1989, labelled Well A, that was drilled off the flank of the culmination. The bottom-hole location for the proposed well is marked Well B on this same figure.

#### 4.3.1 Drilling Well B

Well B was spudded from a surface location Northeast of the of the bottom-hole target. The processed versions of the Response data set available at the time of picking the location were poststack time migration (Figure 4.5), prestack time migration (Figure 4.6), and prestack depth migration (Figure 4.7). The prestack time and depth migrations improved reflector continuity on the flank of the structure, but no appreciable shifts in the seismic event at the

target location were visible among the three different versions, as shown by the marker for Well B in Figures 4.5-4.7.

The primary seismic marker used in structural mapping in this area is the Jurassic Nordegg and the primary and secondary targets are presumed to be conformable above and below the Nordegg. The Nordegg reflector was targeted for the location marked Well B in Figure 4.7, approximately 200 m back from the termination of the Nordegg reflector on this section (Figure 4.7). The well trajectory followed its proposed course, but at 3243 m depth, it was obvious from the samples from drilling that Well B had missed the main target.

Two courses of action followed: (1) a dipmeter was run from surface casing to total depth of the well and (2) the Response data set was reprocessed through ADM. In deriving the velocity model, several migrations using epsilon values ranging from 0.025 to 0.3 were compared to find the maximum reflector amplitude and continuity of reflection for the deeper reflectors as prescribed by Vestrum et al. (1999). The final ADM section is shown in Figure 4.8.

Results of the ADM showed the Nordegg reflector in a position up to 250 m southwest depending on depth and lateral position relative to the triangle-zone dips (Figure 4.8). Results of the dipmeter survey confirmed that Well B had been drilled off the leading edge of the structure. Dips up to  $70^\circ$  were encountered near the bottom of the hole. A new trajectory 175 m to the southwest was chosen from the ADM and confirmed by dipmeter analysis.

The sidetrack was drilled from 2754 m to 3382 m TD and again logged by dipmeter. The sidetrack encountered the natural-gas-producing formations predicted by the ADM processing and low dips, indicating that the sidetrack was near the crest of the structure, which again correlates well with the ADM section (Figure 4.8). Note also in Figure 4.8 that the new position of the structure creates a better tie between the seismic events and the dipmeter from Well A.

#### **4.3.2 Discussion**

Although prestack time migration and prestack depth migration are considerable steps forward in thrust-belt seismic processing, ignoring seismic anisotropy in a dipping clastic overburden can lead to significant lateral-position errors on seismic data. In this case, the



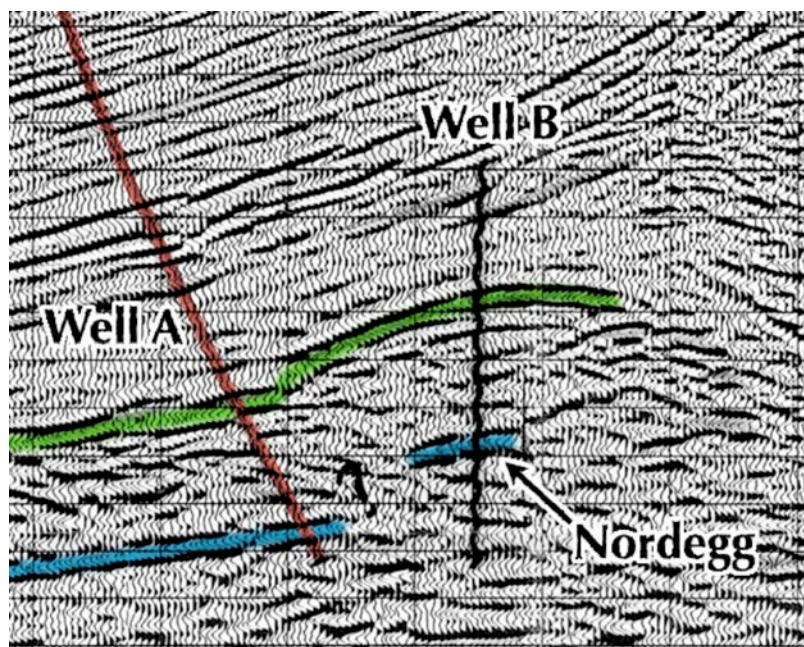


Figure 4.5 Poststack time migration of the Response data set showing Nordegg reflector and proposed location for Well B.

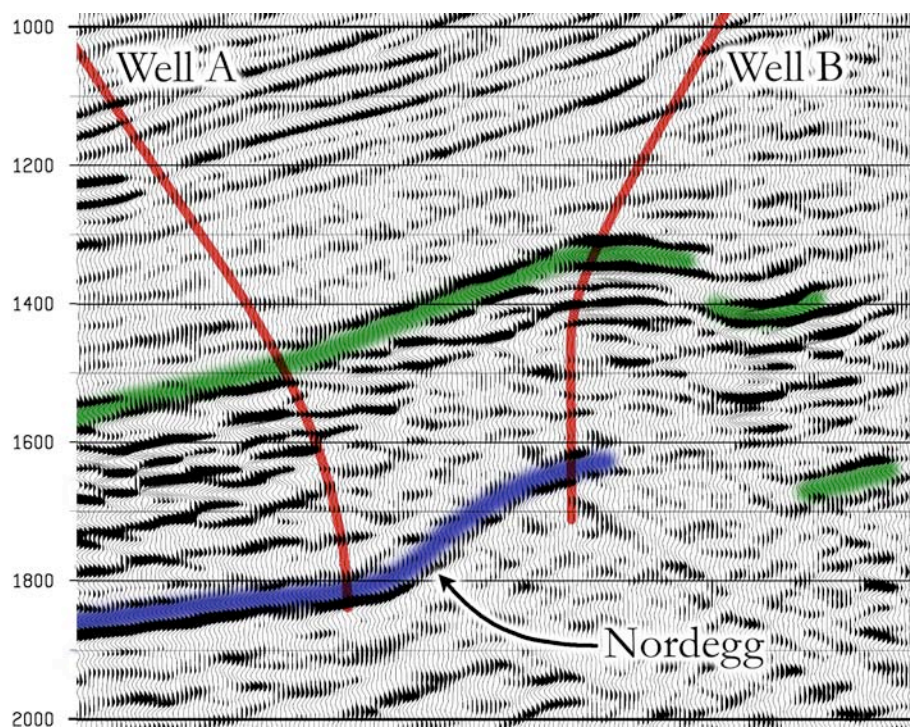


Figure 4.6 Prestack time migration of the Response data set showing well trajectories for Well A and Well B.



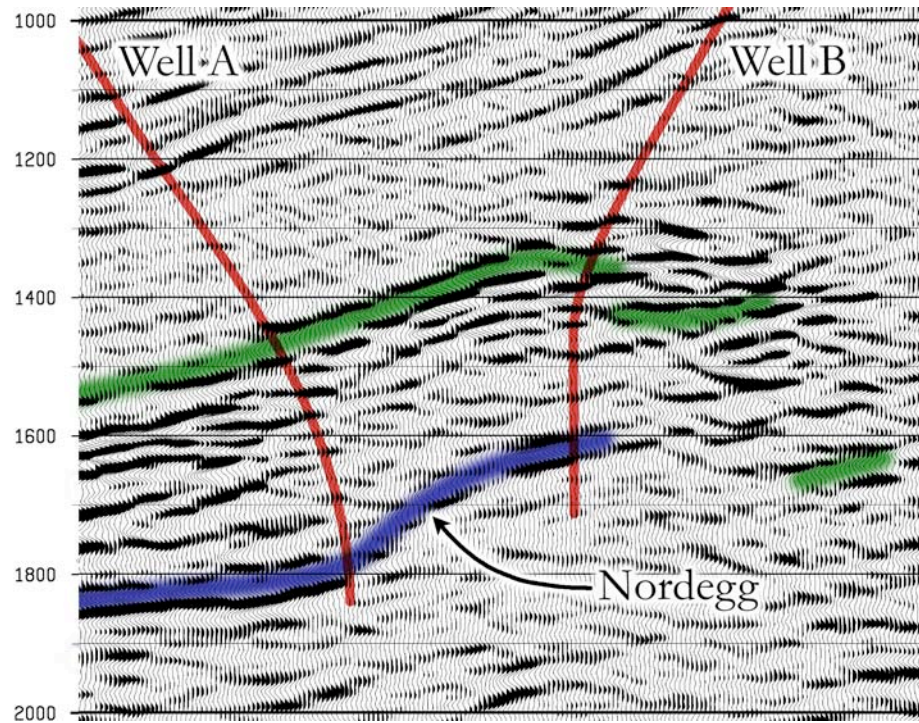


Figure 4.7 Prestack depth migration displayed in time with well trajectories.

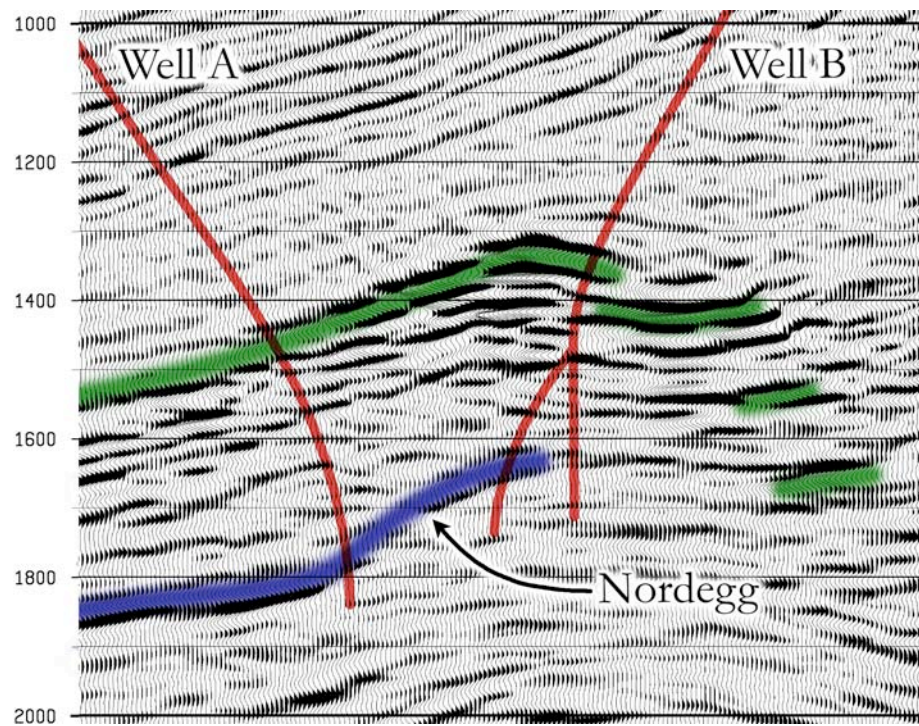


Figure 4.8 Prestack anisotropic depth migration displayed in time showing well trajectories for Well A and Well B and the sidetrack of Well B.

well trajectory crossed horizontal seismic reflections and encountered 70° northeast dips due to the lateral mispositioning of reflectors. The position of the reflectors on the ADM section provides a better correlation between seismic and well data in both wells. In the process of testing the algorithm, the technology was applied to a natural-gas drilling problem, resulting in a successful natural-gas development well.

Velocity analysis in complex-structure areas is highly interpretive and underconstrained, considering the parameters needed for optimum imaging and position of structures below the anisotropic clastic overburden. Any preprocessing that will improve the signal quality of the data prior to migration will prove valuable in obtaining optimum velocities and an optimum final image. Noise-suppression methods will prove highly valuable in this application.

Statics, in contrast, represent a potentially dangerous preprocessing application before depth migration. The most accurate depth migration will raytrace from the source and receiver elevations on the rough topographic surface instead of raytracing from some sort of datum and migrating data with elevation statics correction. Weathering statics, static corrections for near-surface velocity variations, may improve the image, but should be tested. Reflection statics, static corrections that maximize the cross-correlation or similarity between traces, may attempt to correct for velocity effects in the seismic data for which depth migration should correct. If the reflection-statics correction and depth-migration each correct for the same velocity effect, then the resulting overcorrection will result in a degradation of image quality. If one assessed a need for reflection statics to correct for misalignment of traces due to near-surface variations that depth migration and weathering statics cannot correct for, then reflection statics should be calculated on seismic data with offset corrections applied using moveout corrections based on the same traveltimes used in the anisotropic depth migration.

## 4.4 Conclusions

Field studies were compiled to test the algorithm on exploration seismic data. These field studies show improvements in imaging and structural-position accuracy over traditional migration algorithms when anisotropy corrections are applied.

The Benjamin Creek example showed dramatic improvements in imaging complex

structures when the overburden dip changes abruptly across a fault plane. In a more robust setting for seismic imaging, the Triangle Zone dataset showed subtle imaging improvements with more accurate lateral and vertical positioning of seismic reflectors. With the potential of improved structural positioning on seismic data, an oil-industry explorationist applied anisotropic depth migration after missing a natural-gas exploration target. The resulting seismic section agreed with another independent measurement, the dipmeter data from the well, and the revised drilling strategy guided the well trajectory to the natural-gas reservoir.

Accounting for velocity anisotropy in seismic migration yields a more accurate model of the subsurface velocities, improved structural positioning and reflector imaging, and accurate depths without additional depth scaling after migration. Anisotropic depth migration improves the accuracy of the seismic image and can reduce risk in foothills exploration.



## Chapter 5

# Conclusions

Seismic anisotropy in dipping clastics prevalent in complex-structure geologic environments causes imaging and position problems on surface seismic data. A velocity-model definition that includes a description of the seismic anisotropy and an anisotropic migration algorithm are needed to reduce the effects of anisotropy on seismic images. To propagate our velocity model with accurate velocity anisotropy parameters, we also need anisotropic velocity-model-building methodologies. Once these tasks are completed, the effectiveness of anisotropic depth migration may be demonstrated on complex-structure land data from the Alberta Foothills.

My investigation of position problems on seismic images showed that the lateral position error below dipping clastics is as high as the thickness of the overburden multiplied by the fractional difference between the normal-to-bedding velocity and the parallel-to-bedding velocity when the overburden dip is near  $45^\circ$ . During this investigation of lateral-position error, I also discovered that this sideslip error can change significantly with offset, potentially creating a significant reflection-point smear problem. Raytracing predicted that the reflection-point smear can be even larger than the maximum sideslip error when the dip of the anisotropic overburden is near  $20^\circ$  or  $65^\circ$ . Imaging problems caused by reflection-point smear and position problems from sideslip show the need for anisotropic corrections in depth migration applicable for any dip in the clastic overburden between from  $10^\circ$  to  $80^\circ$ .

Before we can correct for seismic anisotropy in depth migration, we need a subsurface model definition that describes the velocity as it varies with direction and indicates the orientation of the fast and slow velocity directions, i.e., the bedding dip. I chose a parameterization scheme as defined in Section 2.1 of this volume.

After defining the anisotropic velocity model, I coded anisotropic corrections into a seismic traveltime calculator used in Kirchhoff depth migration of complex-structure land seismic data. Testing of the resulting anisotropic depth migration algorithm included migrating physical-model seismic data and comparing the imaged depth and lateral position of the

seismic reflectors to those of the physical model. Positive test results lead me to take the algorithm to the next step and apply the migration to seismic data from the Alberta Foothills.

When depth migrating seismic data, we do not know the velocity model before we migrate. We must then take an iterative approach to depth migration where we estimate velocities, migrate with those velocities, calculate velocity errors, update the velocity model, and migrate again. In anisotropic depth migration, I took the same approach in velocity model-building, using traditional velocity-analysis methods to interpret the subsurface velocity model and to detect errors in the velocities and velocity anisotropy parameters. These traditional velocity-analysis methods included moveout analysis on migrated image gathers and coherency analysis on migrated stack images. Anisotropic velocity model building is highly interpretive and a depth-imaging practitioner must use all diagnostics at his or her disposal and make a velocity-model interpretation based on indicators from the diagnostics. The interpreted velocity model is then used in an anisotropic depth migration and the migrated output is once again put through the gamut of velocity diagnostics to determine if further updates are required or if the velocity model is deemed sufficiently accurate for the exploration objective of the seismic data.

Using the algorithm and velocity analysis methods defined for and described in this thesis, I applied anisotropic depth migration to three seismic datasets from the Alberta Foothills in Western Canada. The first, a public-domain dataset from Benjamin Creek, Alberta, showed considerable improvements in the final image over previous isotropic depth migration with the application of anisotropic depth migration. The second dataset showed subtle improvements in the detailed imaging of complex fold structures and the seismic depth showed a close correlation with the depth observed in the well when anisotropy corrections were included in the migration. The third data example was from an exploration case history where anisotropic depth migration was used to get a more accurate position for an exploration target during drilling.

## References

- Alkhalifah, T. and Larner, K., 1994, Migration error in transversely isotropic media: *Geophysics*, **59**, 1405-1418.
- Alkhalifah, T., 1995, Gaussian beam depth migration for anisotropic media: *Geophysics*, **60**, 1474-1484.
- Ball, G., 1995, Estimation of anisotropy and anisotropic 3-D prestack depth migration, offshore Zaire, *Geophysics* **60**, 1495-1513.
- Brown, R. J., Lawton, D. C. and Cheadle, S. P., 1991, Anisotropic physical modelling of multioffset profiles over an orthorhombic medium: 53rd Mtg., EAEG, 546-547.
- Chen, J. and Schuster, G. T., 1999, Resolution limits of migrated images: *Geophysics, Soc. Of Expl. Geophys.*, **64**, 1046-1053.
- Dai, N., Cheadle, S., and Isaac, J.H., 1998, Prestack depth migration in TI media: examples with numerical and physical model data, GEOTRIAD '98, Joint meeting of CSEG, CSPG, and CWLS.
- Dellinger, J., 1991, Anisotropic seismic wave propagation, PhD thesis, Stanford University.
- Dellinger, J. and Vernick, L., 1994, Do traveltimes in pulse-transmission experiments yield anisotropic group or phase velocities? (short note): *Geophysics* **59**, 1774-1779.
- Di Nicola-Carena, E., 1997, Solving lateral shift due to anisotropy: SEG 67th Ann. Mtg., , Expanded Abstracts, 1525-1528.
- Etris, E.L., Crabtree, N.J., Dewar, J., 2001, True depth conversion: More than a pretty picture: *CSEG Recorder* **26**, 11-22.
- Fei, T., Dellinger, J., Murphy, G.E., Hensley, J.L., and Gray, S.H., 1998, Anisotropic true-amplitude depth migration, GEOTRIAD '98, Joint meeting of CSEG, CSPG, and CWLS.
- Ferguson, R.J., and Margrave, G.F., 1998, Depth migration in transversely isotropic media by nonstationary phase shift, GEOTRIAD '98, Joint meeting of CSEG, CSPG, and CWLS.
- Gibson, R.L., Jr., Sena, A.G., and Toksöz, M.N., 1991, Paraxial raytracing in 3D inhomogeneous, anisotropic media. *Geophysical Prospecting* **39**, 473-504.
- Gray, S.H., 1997, Seismic imaging: use the right tool for the job, *Leading Edge* **16**, 1585-1588.
- Hagedoorn, J.G., 1954, A process of seismic reflection interpretation: *Geophysical Prospecting*, **2**, 85-127.
- Ha, J., 1986, Wave propagation in transversely isotropic and periodically layered isotropic media, *Geophys. J. R. astr. Soc.* **86**, 635-650.

- Hake H., Helbig, K. and Mesdag, C.S., 1984, Three-term Taylor series for  $t^2 - x^2$  curves over layered transversely isotropic ground, *Geophysical Prospecting* **32**, 828-850.
- Isaac, J.H. and Lawton, D.C., 1999, Image mispositioning due to dipping TI media: A physical seismic modeling study: *Geophysics* **64**, 1230-1238.
- Larner, K.L. and Cohen, J.K., 1993, Migration error in transversely isotropic media with linear velocity variation with depth, *Geophysics* **58**, 1454-1467.
- Leslie, J.M., Lawton, D.C., Cunningham, J.D., 1997, A refraction seismic field method to determine the anisotropic parameters of Wapiabi shales, CSEG 1997 National Mtg.
- Leslie, J.M., and Lawton, D.C., 1998, Depth migration of anisotropic physical model data, GEOTRIAD '98, Joint meeting of CSEG, CSPG, and CWLS.
- Lines, L, Wu, W., Lu, H., Burton, A. and Zhu, J., 1996, Migration from topography: Experience with an Alberta Foothills data set: *Can. J. Expl. Geophys.* **32**, 24-30.
- Love, A.E.H., 1944, A treatise on the mathematical theory of elasticity: 4th ed., Dover Publ. Inc.
- Markham, M.F., 1957, Measurement of elastic constants by the ultrasonic pulse method, *Brit. J. Appl. Phys.*, suppl 6, 56-63.
- Musgrave, M.J.P., 1959, The propagation of elastic waves in crystals other anisotropic media, *Rep. Prog. Phys.* **22**, 74-96.
- Musgrave, M.J.P., 1970, *Crystal Acoustics*, Holden-Day.
- Phadke, S., Kapotas, S., Dai, N., and Kanasewich, E.R., 1994, Migration of P-wave reflection data in transversely isotropic media: *Geophysics*, **59**, 591-596.
- Postma, G. W., 1955, Wave propagation in a stratified medium: *Geophysics*, **20**, 780-806.
- Schmid, R., Butler, P., and Rennie, B., 1998, Practical anisotropic depth imaging, GEOTRIAD '98, Joint meeting of CSEG, CSPG, and CWLS.
- Schultz, P. and Canales, L., 1997, Seismic velocity model building: CE in Dallas, 2 November: *The Leading Edge* **16**, 1063-1064.
- Schultz, P. S. and Sherwood, J. W. C., 1980, Depth migration before stack: *Geophysics*, **45**, 376-393.
- Sena, A. G. and Toksoz, M. N., 1993, Kirchhoff migration and velocity analysis for converted and nonconverted waves in anisotropic media: *Geophysics*, **58**, 265-276.
- Sheriff, R., 1991, *Encyclopedic Dictionary of Exploration Geophysics*: Soc. Expl. Geophys.
- Shuvalov, L.A., 1981, *Modern Crystallography IV: Physical Properties of Rocks*, Springer.
- Stolt, R. H., 1978, Migration by Fourier transform : *Geophysics*, **43**, 23-48.
- Stork, C., Welsh, C. and Skuce, A., 1995, Demonstration of processing and model building methods on a real complex structure data set: *Ann. Conv., Workshop #6, Soc. Expl. Geophys., Proceedings*.

- Thomsen, L., 1986, Weak elastic anisotropy: *Geophysics*, **51**, 1954-1966.
- Tsvankin, I. and Thomsen, L., 1994, Nonhyperbolic reflection moveout in anisotropic media: *Geophysics*, **59**, 1290-1304.
- Uren, N. F., Gardner, G. H. F. and McDonald, J. A., 1990, The migrator's equation for anisotropic media: *Geophysics*, **55**, 1429-1434.
- Uzcategui, O., 1995, 2-D depth migration in transversely isotropic media using explicit operators: *Geophysics*, **60**, 1819-1829.
- Vernik, L. and Liu, X., 1997, Velocity anisotropy in shales: A petrophysical study, *Geophysics* **62**, 521-532.
- Vestrum, R.W., 2001, Exploration applications of seismic velocity anisotropy: 2001 Natnl. Mtg., Can. Soc. Expl. Geophys.
- Vestrum, R.W., 2002, 2D and 3D anisotropic depth migration case histories: 2002 Natnl. Mtg., Can. Soc. Expl. Geophys.
- Vestrum, R.W., and Lawton, D. C., 1999, Anisotropic depth migration: Reducing lateral-position uncertainty of subsurface structures in thrust-belt environments: 69th Annual Internat. Mtg., Soc. Expl. Geophys.
- Vestrum, R.W., and Lawton, D. C., 2000, Dip-oriented imaging: Anisotropy and directionality in the prestack domain: GeoCanada 2000 convention, Calgary, Canada.
- Vestrum, R.W., and Muenzer, K., 1997, Anisotropic depth imaging below dipping shales, CSEG 1997 National Mtg.
- Vestrum, R.W., Schmid, R., and Lawton, D.C., 1998a, Anisotropic imaging assumptions: Don't forget the dip, GEOTRIAD '98, Joint meeting of CSEG, CSPG, and CWLS.
- Vestrum, R.W., Schmid, R., and Lawton, D. C., 1998b, Determining parameters for seismic imaging in dipping anisotropic strata: 68th Annual Internat. Mtg., Soc. Expl. Geophys., Expanded Abstracts, 1289-1292.
- Vestrum, R.W., Lawton, D.C., and Schmid, R., 1999, Imaging structures below dipping TI media, *Geophysics* **64**, 1239-1246.
- Vestrum, R.W., Callahan, C., and Lawton, D. C., 2001, An Exploration Case History: Anisotropic Depth Migration in the Central Alberta Foothills: 2001 Natnl. Mtg., Can. Soc. Expl. Geophys.
- Vestrum, R.W., Mackie, D.J., and Schoepp, A., 2003, To drill or not to drill: Seeking untapped thrust-fault structures using 3D ADM in Blackstone, Alberta: 2003 Natnl. Mtg., Can. Soc. Expl. Geophys. and Can. Soc. Pet. Geol.
- Yilmaz, O., 1987, *Seismic Data Processing*, SEG press.
- Zhu, J., Lines, L. and Gray, S., 1998, Smiles and frowns in migration/velocity analysis: *Geophysics*, Soc. of Expl. Geophys., **63**, 1200-1209.